Technische Universität München

TECHNISCHE UNIVERSITÄT MÜNCHEN
Max-Planck-Institut für extraterrestrische Physik

Using Gamma-ray Bursts to Probe the Cosmic Intergalactic Medium

Vladimir Sudilovsky

Vollständiger Abdruck der von der Fakultät für Physik der Technischen Universität München zur Erlangung des akademischen Grades eines

Doktors der Naturwissenschaften (Dr. rer. nat.)

genehmigten Dissertation.

Vorsitzender:		Univ.-Prof. Dr. Alejandro Ibarra
Prüfer der Dissertation:	1.	Priv.-Doz. Dr. Jochen Greiner
	2.	Univ.-Prof. Dr. Lothar Oberauer

Die Dissertation wurde am 12.02.2014 bei der Technischen Universität München eingereicht und durch die Fakultät für Physik am 28.05.2014 angenommen.

Abstract

Gamma-ray bursts (GRBs) rapidly liberate enormous amounts of energy through the cataclysmic destruction of an individual massive object. GRBs are the most energetic events in the Universe, boasting isotropic equivalent energy releases of $E \sim 10^{51-54}$ erg in time scales of seconds – more energy than even active galaxies in the same timeframe. These transient events represent the ultimate high energy laboratories, and their afterglows are readily detectable from ground-based observatories out to cosmological distances out to $z \sim 8$. For this reason, GRBs are a natural tool to probe the early universe. To this end, programs to quickly measure the photometric and spectroscopic properties of GRB afterglows are providing a wealth of data that enable us to characterize the physical properties of both the burst itself and its host environment.

In addition to providing extremely poignant information on the burst and its medium, GRB afterglow spectra show the presence of matter intervening along the line of sight. MgII , an important tracer of α-element processes and thus of star formation and galaxies, has been measured in $\sim 60\%$ of GRB afterglow spectra. Surprisingly, MgII is only found in $\sim 30\%$ of quasar spectra. This discrepancy in the number density dn/dz of intervening MgII absorbers implies that there are significant observational biases in either the spectroscopic samples of either GRB afterglows or quasars.

In this work, we review the MgII issue and the biases proposed to explain it. We find that observations of other tracer systems (namely CIV) do not show the same overdensity, and thus conclude that solution to the MgII problem is related to the geometry of the sight-line relative to the absorbers. We conclude that an observational bias stemming from dust extinction arising from MgII cannot explain such a large discrepancy. Finally, we search for a signal of the MgII discrepancy in the transverse direction by computing the GRB-galaxy two point correlation function using five years of data collected by the GROND instrument at La Silla Observatory, Chile.

We find no signal of the MgII issue in the correlation function, suggesting that this issue exists past the sensitivity limits of current samples of afterglow images. Since spectroscopy is generally more observationally difficult to perform than imaging, we conclude that the biases responsible for the MgII issue do not affect GRB afterglow imaging. Combining imaging and spectroscopic data may be a viable, albeit observationally expensive, route on which to definitively solve the MgII issue.

Zusammenfassung

Gammastrahlungsausbrüche (GRBs) setzen innerhalb kurzer Zeit durch kataklysmische Zerstoerung einzelner massereicher Sterne riesige Energiemengen frei. GRBs sind mit isotropen Äquivalentenergien von $E \sim 10^{51-54}$ erg, die innerhalb von Sekunden abgestrahlt werden, die energiereichsten Ereignisse im Universum, auch im Vergleich zu den Kernen aktiver Galaxien. Diese Ausbrüche stellen in vieler Hinsicht die ultimativen Laboratorien zum Studium hoch-energetischer Prozesse dar. Das Nachleuchten, sog. afterglows, ist bis in kosmologische Entfernungen von $z \sim 8$ relativ leicht von bodengebundenen Observatorien messbar. Aus diesem Grund stellen GRBs ein offensichtliches Werkzeug zum Studium des frühen Universums dar. Die entsprechenden Programme zur Messung der photometrischen und spektroskopischen Eigenschaften des Nachleuchtens liefern eine Füelle von Daten, die es uns ermöglichen, die physikalischen Eigenschaften sowohl des GRB als auch der umgebenden Muttergalaxie zu charakterisieren.

Zusätzlich zu diesen Informationen zeigen Spektren des Nachleuchtens auch Signaturen von Materie entlang unserer Sichtlinie zum GRB. MgII, ein wichtiger Indikator von α-Element Prozessen und damit Sternentstehung in Galaxien, ist in 60% aller Spekten gefunden worden. Im Gegensatz dazu findet sich MgII nur in 30% der Spektren von Sichtlinien zu Quasaren, besonders leuchtkräftigen Kernen aktiver Galaxien. Diese Diskrepanz in der Anzahldichte dn/dz der MgII-Absorber entlang der Sichtlinien impliziert, dass es signifikante systematische Messabweichungen gibt, entweder in der GRB- oder aber der Quasar-Stichprobe.

In dieser Arbeit wird das MgII Problem und die möglichen Ursachen untersucht. Wir haben entdeckt, dass ein anderer Indikator (nämlich CIV) diese Überdichte nicht zeigt, und schlussfolgern deshalb, dass das MgII Problem mit der Geometrie der Sichtlinien relativ zu den Absorbern zusammenhängt. Absorption durch Staub kann eine solch grosse Diskrepanz nicht erklären. Wir haben deshalb nach einem Signal der MgII Überdichte zu GRBs in transversaler Richtung gesucht, indem wir die GRB-Galaxien Korrelationsfunktion gemessen haben. Dazu benutzen wir Daten aus 5 Jahren GRB-Messungen mit dem GROND-Instrument auf der Sternwarte in La Silla, Chile.

Allerdings finden wir in der Korrelationsfunktion kein Signal der MgII Üeberdichte. Dies legt nahe, dass die gegenwärtigen Bilddaten der GRB Stichprobe nicht empfindlich genug sind, um Aussagen üeber das MgII Problem treffen zu können. Da Spektroskopie im allgemeinen beobachtungstechnisch schwieriger ist als Photometrie, bedeutet dies, dass die fuer die MgII Überdichte verantwortlichen Messeffekte die GRB Photometrie nicht beeinflussen. Eine zukünftige Kombination von photometrischen und spektroskopischen Daten könnte ein gangbarer, wenn auch aufwändiger Weg sein, um das MgII Problem definitiv zu lösen.

Contents

Chapter 1

Introduction

1.1 Fundamental Observational History of γ-ray Bursts

Starting in 1963, the US Air Force launched a series of satellites designed to detect γ and x-ray photons produced by man-made nuclear detonations (Dickinson & Tamarkin 1965; Singer 1965). These satellites, named *Vela* after the Spanish word *Velador*, or "watchman", had a time resolution of $\sim$ 0.2s, whereas the light travel time across the orbital diameter was $\sim$1 second. The delay time between three or more satellites detecting the same trigger allowed an angular resolution of $\sim$10 degrees. A post-facto study of 16 triggers detected by the Vela satellites between July 1969 and July 1972 revealed that these events did not occur at the Sun, Moon, or Earth (Klebesadel et al. 1973). Shortly thereafter, Cline et al. (1973) measured the events' high energy spectra, noting that the peak energy was indeed in the γ regime. These sources were subsequently dubbed "cosmic gamma-ray bursts" (GRBs). GRBs are named after the ISO-date on which they are detected, and sequentially enumerated with an English letter in the case of multiple events detected on the same date: GRB 670702 is the first GRB detected by mankind, observed on July 7, 1967. The γ lightcurve of this burst is presented in Fig. 1.1.

Unsurprisingly, the characterization and modeling of this new class of astronomical event became a top priority for the research after the announcement of their discovery. To this end, many satellites sensitive to γ-rays were incorporated into an InterPlanetary Network (IPN), increasing angular resolution proportional to the IPN's physical size. In Fig. 1.2, Vedrenne (1991) present the spatial distribution of 171 GRBs detected by the IPN (Atteia et al. 1987) and Konus (Mazets et al. 1981), a standalone mission that localized GRBs using flat detectors. The distribution of GRBs is consistent with being isotropic in this dataset. Though this result intuitively implies an extra-galactic origin, the detectors at the time had only a $\sim$50% localization efficiency – they could localize only the brighter subset of detections. With this in mind, the isotropic distribution could have also be interpreted as detecting only those bursts that are very close to our position in the Milky Way. A further support for this interpretation is that, at the time, the number distribution of events as a function of their flux (logN-logS) seemed to flatten

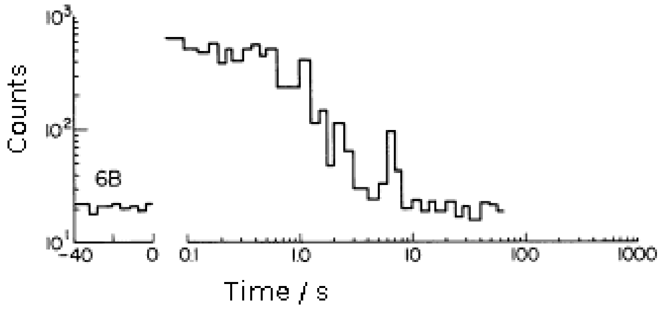

Figure 1.1 Prompt emission γ-ray light curve of the first ever GRB that was detected by the *Vela* satellites.

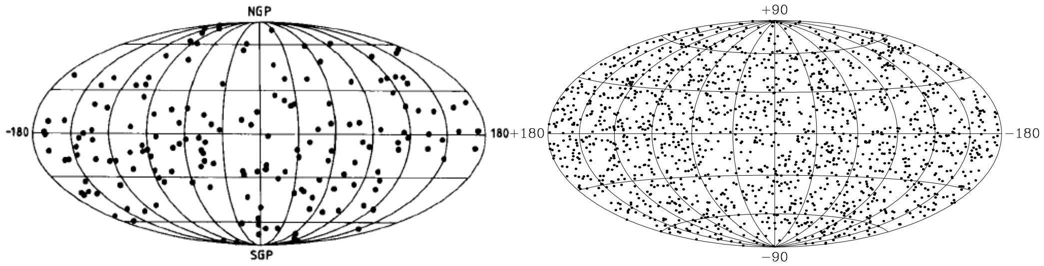

Figure 1.2 **Left:** Spatial distribution of 171 GRBs detected by the KONUS experiment and the IPN, the two main catalogs of GRBs in the 1980s. Only bursts with high detection significance could be localized, corresponding to a ~50% localization rate. **Right:** Spatial distribution of 1005 GRBs detected by BATSE. All bursts that were detected were localized to within a few degrees.

at lower fluxes, whereas cosmologically distributed objects (with a luminosity function that varies only mildly) should not deviate from a $-3/2$ slope (Strong & Klebesadel 1974).

Another important consideration were the apparent energies at which these events were observed. These events were observed with fluences at 10^{-4}erg cm^{-2}, which is orders of magnitudes larger than even active galaxies. The peak energy was clearly non-thermal and peaking in the γ-regime. With such large apparent energies, theoretical modeling at the time could not account for such large absolute energies if the events were cosmological in origin. Furthermore, the observed time variability on the order of milliseconds required a compact progenitor due to light travel time across the event. Naturally, energy injection onto neutron stars having strong intrinsic magnetic fields was a popular model during this time.

The Compton Gamma-Ray Observatory (CGRO), specifically designed to study GRBs, was launched in 1991. The Burst and Transient Source Experiment (BATSE)

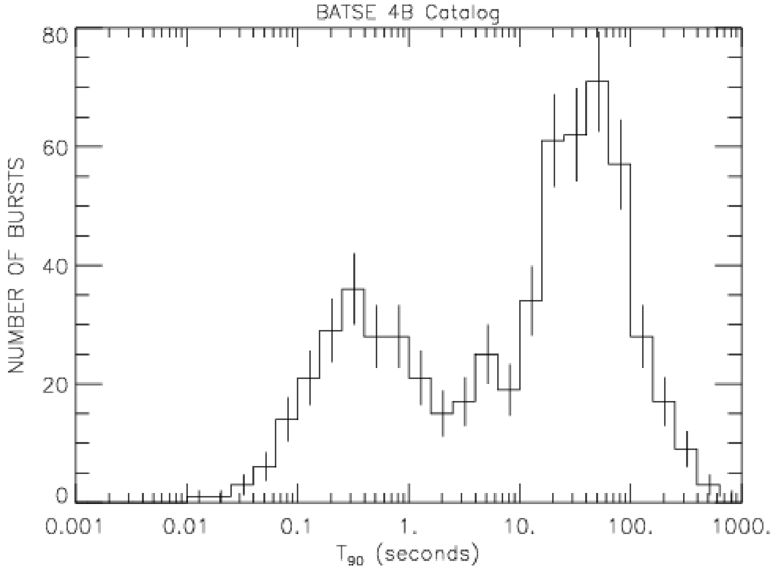

Figure 1.3 The temporal distribution of GRBs detected by BATSE. The events follow a bi-modal distribution separated at $T_{90} \sim 2$s, where T_{90} is the duration during which 90% of the γ flux is observed.

was the main GRB detector, boasting an effective area and sensitivity an order of magnitude higher relative to previous missions. These properties enabled BATSE to record on average one GRB per day, increasing the sample of GRBs by an order of magnitude in just a few years of operation. In Fig. 1.2, the spatial distribution of 1005 GRBs detected by BATSE are presented (Briggs et al. 1996). The increased localization efficiency of BATSE relative to prior missions confirmed that even low luminosity GRBs are isotropically distributed. Additionally, the BATSE catalog showed strong evidence for a bimodal temporal distribution of GRB afterglows, as presented in Fig. 1.3 (Fishman et al. 1994). BATSE also showed that the long duration class of bursts were generally had spectra that were generally dominated by lower energy X-rays as compared to the harder, high energy dominated shorter bursts.

Though the undeniable isotropy of triggers shown by BATSE suggests a cosmological origin of GRBs, the confirmation and acceptance of this theory came as a result of the discovery of the GRB afterglow and the measurement of its spectrum. The satellite BeppoSAX was launched with the goal of providing rapid and accurate localizations of GRBs – criteria that previous missions such as the IPN and CGRO could accomplish only one or the other of. BeppoSAX fulfilled its design goal after it discovered the first fading x-ray afterglow of a GRB. GRB 970228 was observed with the Medium Energy Concentrator Spectrometer (2-10 keV) aboard BeppoSAX and an uncatalogued x-ray source was localized to within $3'$ within eight hours of the initial trigger (Costa et al. 1997b). Subsequent observations showed that this source faded, and later the

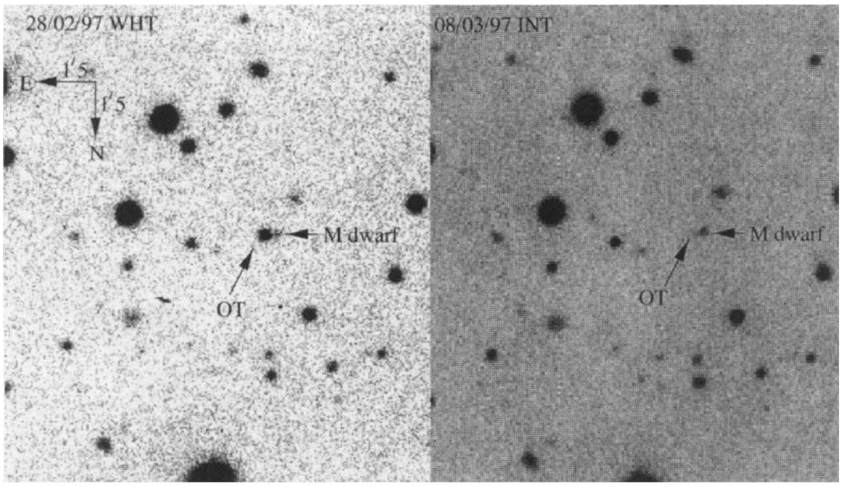

Figure 1.4 Images from the William Herschel Telescope at $\Delta t = 1$ day (left) and the Isaac Newton Telescope (right) at a $\Delta t = 9$ days after the initial trigger. The afterglow of GRB 970228 is indicated as "OT" (Optical transient).

localization was confirmed by the IPN (Hurley et al. 1997). Fig.1.4 presents the optical images of a GRB afterglow (van Paradijs et al. 1997). This discovery set the precedence for the multi-wavelength rapid follow-up of GRB triggers. Indeed, two months after the ground breaking observations of GRB 970228, BeppoSAX detected and localized GRB 970508 (Costa et al. 1997a). This burst's optical afterglow spectra was measured with the Keck Telescope, and absorption lines of FeII , MgI and MgII at redshifts $z = 0.767$ and $z = 0.835$ were detected (Metzger et al. 1997). These observations definitively showed that the GRB must have occurred at $z \geq 0.835$, thus proving the cosmological origin of GRBs.

The next major missions responsible for advancing our understand of GRBs are the High Energy Transient Explorer (HETE/HETE-2) and Swift gamma-ray burst mission (*Swift*) (Ricker et al. 2003; Gehrels et al. 2004). Following the astounding success of BeppoSAX, these new missions were designed to improve the response time between the GRB trigger and its localization and follow-up with other instruments. HETE/HETE-2 is responsible for establishing the connection between GRBs and supernovae Type Ic (SN Ic), and thus constraining possible progenitor models and their underlying explosion physics.

1.2 Standard Model

1.2.1 Fireball model and shocks

The standard model for GRBs and their afterglows has developed since the discovery of their cosmological origins. As mentioned in 1.1, the variability of an astronomical source is expected to constrain its size by $R < c\Delta t$, where R is the sources size, c is the speed of light, and Δt is the shortest time variability observed. This relationship stems from the a priori assumption that if the light crossing time is longer than the intrinsic variability, the observed variability is much slower as a result of it being smeared out by asynchronous emission from different regions. By this argument, the region responsible for the prompt γ emission must be on order 10^3 kms, meaning that GRBs come from a single astrophysical source. The time-integrated energy release of $10^{51} - 10^{53}$ erg is released in typically a few seconds, and the cosmological distances at which the bursts occur require even larger absolute energies. For comparison, this is 4-6 orders of magnitude larger than the energy output of our Sun during its entire lifetime. This last property is a strong reason to adopt the model in which the energy is beamed rather than emitted isotropically. This concept of a beamed "fireball" was introduced relatively early during the history of GRBs, as similar explosions had already been observed in SNe (Cavallo & Rees 1978).

An important observational constraint for this fireball model is the observation of significant flux above 1 MeV (Matz et al. 1985). These observations require that electron-positron pair creation is suppressed, as this would deplete the population of γ photons above 1.022 MeV. The energy requirements coupled with the preference for beamed emission naturally leads to a very high rate of pair production, as the density of high energy photons would be very high. Such an environment would be well above the Eddington luminosity, causing a rapid relativistic expansion as long as the baryonic loading is low (Paczynski & Proszynski 1986). A relativistically expanding beam would then alleviate the problem of not observing signatures of pair production:

- Observed photons are blue-shifted, reducing the intrinsic population of photons of sufficient energy for pair creation

- The area of the emitting region is increased by a factor by the square of its Lorentz factor Γ^2, lowering the density of γ photons within the fireball

Piran (1999); Lithwick & Sari (2001); Mészáros (2002) calculated that such a relativistic beam would become optically thin to pair production if $\Gamma \gtrsim 100$, for a typical power-law photon index $\alpha \sim 2$ ($dN_\gamma/dE \propto E^{-\alpha}$).

In such a relativistically expanding fireball, the majority of matter is swept up in a thin shell, since it is all traveling at $v \sim c$. The emission from such a thin shell is expected to be quasi-thermal, which is not observed. Additionally, the timescale that the fireball becomes optically thin is on the order of milliseconds, while GRB emission is typically lasts 10^3 longer, even in its rest frame. To account for these discrepancies Rees & Meszaros (1992, 1994) suggested that the main emission mechanism for prompt emission are internal shocks, in which thin shells with slightly different Lorentz factors overtake each other during jet propagation, and external shocks for the afterglow emission, in which these shells are swept up and interact with the interstellar medium. The predicted evolution of such a fireball is qualitatively depicted in Fig. 1.5.

The shock caused by the interaction of the fireball with the ISM causes shocks that propagate both with and into the blast wave. These are referred to as the forward and

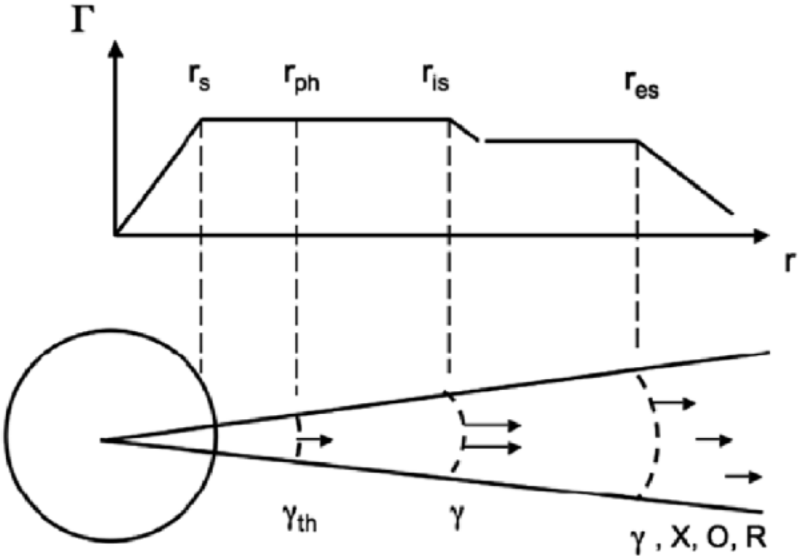

Figure 1.5 Schematic prediction of the GRB fireball's bulk Lorentz factor Γ as a function of its radius. r_s is the radius at which he fireball is no longer accelerated, r_{ph} is the photospheric radius at which the Thompson optical depth approaches unity, r_{is} is the radius at which internal shocks dissipate, and r_{es} is the radius at which the external interstellar medium affects the deceleration and causes the external shocks and thus lower energy emission. Adapted from Mészáros (2006).

reverse components of the external shock respectively, and are expected to contribute to the afterglow evolution in distinct ways. The afterglow emission is expected to increase in intensity until enough of the ISM has been swept up by the blast wave that is starts to decelerate r_{dec}. At this point, the afterglow has reached its intensity maximum and thus begins its temporal (power-law) decay (Mészáros 2006). The external shocks that produce the afterglow emission can be fully characterized by the parameters E_0, ϵ_e, ϵ_B, n, and p, which are the initial energy, fractional energy carried by electrons, fractional energy carried by the magnetic field, ISM density, and spectral index of the accelerated electrons (Panaitescu & Kumar 2000).

1.2.2 Progenitor models

Long GRBs and core collapse

Observations of prompt and afterglow emission impose several strong criteria on the progenitors of GRBs. The short time scales of variability require a single astrophysical object. The beamed energy release of $\sim 10^{52}$ erg imply ultra-relativistic blast waves from this object. Additionally, the spectra show no evidence of hydrogen lines, suggesting that the progenitor's hydrogen envelope was already shed. A very natural progenitor that fulfills these criteria is a Wolf-Rayet star that collapses directly to a black hole after core collapse, first proposed by Woosley (1993). An accretion disk around the resulting black hole would fuel the central engine fireball, of which a significant fraction would come from neutrino annihilation (Woosley 1993). A large angular momentum would expel the H/He envelope of the progenitor, supporting the formation and collimation of a jet with an opening angle of $\sim 10°$, which is the correct order of magnitude for that expected from GRB observations (MacFadyen & Woosley 1999). However, though the association seems very strong, it should be noted that the expected signatures of Wolf-Rayet winds has not been definitively detected in any GRB afterglow spectra.

Short GRBs and merger events

Short GRBs, though expected to have the same internal/external shock powered emission, have significantly different observational properties from long GRBs. Short GRBs have much harder prompt emission, have afterglow emission that is much fainter, and are typically detected only a $z < 1$ (Fox et al. 2005). A significant fraction of short GRB host galaxies are evolved ellipticals with an evolved stellar population. Due to these observations, a popular model for short GRB progenitors is the merger of two compact objects, i.e. neutron stars and/or black holes. This model is supported by the lack of SN associated with short GRBs, and the involved energies. Currently, the hope of detecting gravitational waves from such events is the best expected observational evidence to cement the association of short GRBs to compact object mergers (Berger 2007).

Chapter 2

GRBs as tools

To obtain observational data regarding the properties of the Universe outside of our Local Group, we require numerous strong detections of cosmological sources. In the past half century, normal galaxies have been detected and studied to moderate redshifts $z \lesssim 1.5$ (Adelman-McCarthy et al. 2008; Skrutskie et al. 2006, e.g.), while smaller numbers of galaxies have been detected at higher redshifts using Lyman-alpha absorption (Steidel et al. 1996, Lyman break galaxies) or emissions detection techniques (Lyman-α emitters).

Detecting higher redshift galaxies directly typically requires long exposure times on large telescopes, making the task of sampling these objects observationally very expensive. An object that is typically easier to detect at higher redshifts are quasars. Although quasars are technically a subclass of active galaxies (AGN), in this work we will use the term to more loosely mean any AGN, as the physical processes that power the various classes of AGN are thought to be effectively the same , namely the accretion of matter onto a super-massive black hole (Salpeter 1964; Zel'dovich & Novikov 1964). Quasars typically have luminosities in excess of their host galaxies by several orders of magnitudes, making them correspondingly easier to detect. There are therefore orders of magnitudes more quasars detected at $z > 2$ as compared to galaxies. However, quasars are somewhat exotic objects, as most galaxies do not have an active nucleus. For this reason, galaxies and quasars probe different environments and therefore different properties of the universe.

GRBs are the most recently discovered class of astrophysical object that are readily observable at high redshifts. Unlike galaxies and AGN, determing the redshift of GRBs is usually extremely straightforward. The emission of GRB afterglows has a non-thermal synchrotron spectrum. Lyman-α absorption will significantly reduce the flux up to the wavelength corresponding to the redshift of the burst, creating a visible 'drop' in the power-law. An example of such a redshift determination is presented in Fig. 2.1.

Since GRBs are associated with the death of massive stars, their detection rate can be used to estimate the cosmic star formation rate (SFR). Kistler et al. (2009) have used GRBs to constrain the SFR. Their comparison of GRBs with Lyman-break galaxies and Lyman-α emitters show a significantly more active early universe, suggesting that the

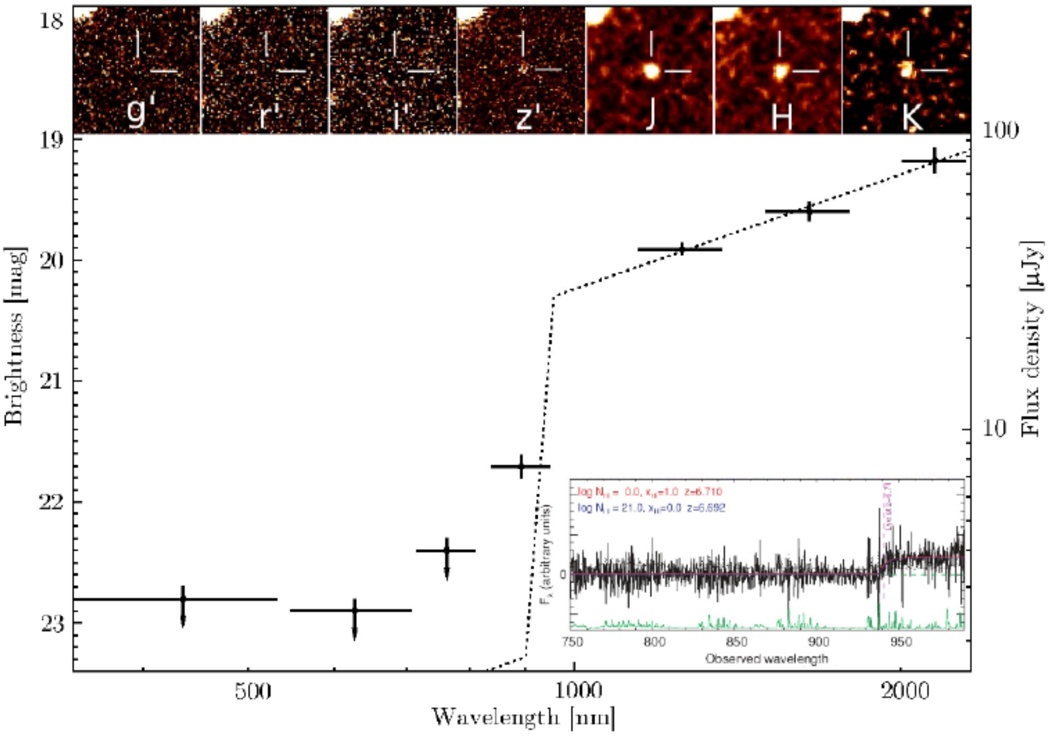

Figure 2.1 Spectral energy distribution of GRB 080913, with spectra and image cutouts in the bottom and top panel, respectively. The best fit photometric redshift from GROND was $z = 6.44 \pm 0.30$, which was later confirmed by VLT/FORS spectroscopy yielding $z = 6.7$. The reduced flux as a result of redshifted Lyman-α absorption is clearly visible in all panels. Adapted from Greiner et al. (2009).

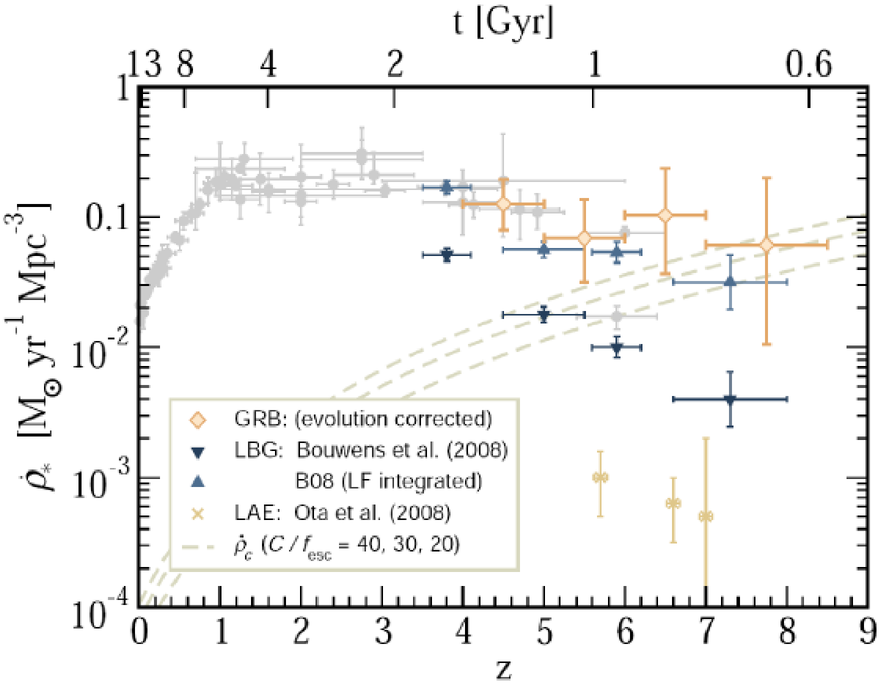

Figure 2.2 The cosmic star formation rate history of the Universe, in solar mass per year per megaparsec. The authors compiled results from Lyman break galaxies, Lyman-α emitters, and GRBs. The critical SFR needed to balance recombination is parametrized and denoted by the gray lines. The SFR as measured by GRBs implies a more active early universe as compared to the other sources. Adapted from Kistler et al. (2009).

universe could have remained ionized even at earlier times. The results of this work are presented in Fig. 2.2. Additionally, progenitors of long GRBs could be Population III stars, the detection of which is a long standing goal of cosmological studies (Bromm & Loeb 2002, 2003).

GRBs originate from a single astrophysical source, and thus provide a probe *into* a distant galaxy. Krühler et al. (2011) used this argument to emphasize that GRB afterglow line-of-sight extinction should not be assumed to be the same as the integrated host galaxy extinction, and that thus GRB host galaxies are likely not especially low mass and dusty. The Damped Lyman-α systems (DLAs) associated with GRB hosts provide a spectroscopic view into a star forming region of a potentially high redshift galaxy. This correlation does not exist for traditionally detected line-of-sight DLAs.

Finally, and most relevantly to this work, GRBs can be thought of as simply bright sources of background light that illuminate matter intervening along its line of sight. With sufficiently high resolution spectroscopy, intervening metal systems can thus be measured. These metal systems provide a unique characterization of the interstellar medium of their hosting galaxies, including the temperature and metallicities. Additionally, since these intervening systems are unrelated to the background source, they should not suffer from the same observational biases when using them to construct a statistical sample.

2.1 The MgII issue

2.1.1 Observational data of MgII

Prochter et al. (2006b) [1] used GRBs to probe the galaxy halos distributed along GRB sight-lines, similarly to what has been done for decades using QSOs. In their study, they identified 14 strong (equivalent width larger than 1 Å) intervening MgII absorbers in the sight-lines of 14 long duration GRBs. The total path-length is $\Delta z = 15.5$ and the mean redshift is $\langle z \rangle = 1.1$, for a mean number density $dn/dz = 0.90 \pm 0.24$. P06's sample includes GRB afterglows observed with high resolution spectrometers at the Las Campanas (HIRES), Keck (MIKE), and Gemini (GMOS) observatories. A summary of P06's GRB sample can be found in Table 2.1. Because the MgII feature is readily detectable with high resolution spectrometers, P06 imposed conservative criteria to construct an instrument-independent search path-length and sample. These criteria are the following:

- The 2796 Å MgII feature must have a rest frame equivalent width of $W_r \geq 1.0$ Å.
- The S/N of a MgII detection must have $> 3\sigma$ significance above background for members of the doublet
- The doublet must be fully resolved, translating to a FWHM $< 500 \mathrm{kms}^{-1}$.
- All MgII doublets detected within 500 km s^{-1} of each other are considered to be one system
- The search region of a given spectrum is limited to within the wavelength range implied by z_{start} and z_{end}, where z_{start} is the maximum of the Lyman-α absorption $\frac{1215.67\times(1+z)}{2796}$ and 0.359[2], and z_{end} is the minimum of 3000 km s^{-1} blue-ward of the GRB and 2.

Prochter et al. (2006a) surveyed and analyzed 7000 MgII absorption lines systems over 50,000 quasars in the SDSS fourth data release (DR4) with the same criteria. P06 compared their independently derived MgII samples and discovered that the MgII systems are detected significantly more frequently in GRBs than in quasars. Assuming Poisson statistics, the 14 MgII absorbers detected in GRB afterglows is different from the mean quasar MgII number density at a significance $> 99.9\%$. This study was repeated with a larger sample by Vergani et al. (2009). After increasing the sample size by a factor of two, the discrepancy remained, although the magnitude of the discrepancy

---

[1] hereafter,P06

[2] To match the SDSS quasar sample

was decreased. Still, the difference between quasar and GRB MgII number densities is different. The cumulative detections of strong intervening MgII found by P06 and Vergani et al. (2009) are presented in Fig. 2.3. The results are consistent with each other to the 2σ level. Additionally, Vergani et al. (2009) showed that the incidence of weaker MgII systems having $0.3 \leq W_r < 1.0$Å is fully consistent in the two classes of sight-lines.

Cucchiara et al. (2013) attempted to extend the sample again by including spectra with significantly lower resolution. They found that the strong MgII excess remains for the high-resolution sample, but the number density reduces to that found in quasars for the lower resolution spectra.

All of these results are extremely surprising. These MgII absorption line systems are distributed by chance along the sight-line to the source, and are not casually linked in any way to the background object. The results, taken at face value, invalidate our current understanding of extragalactic absorption line spectroscopy and analysis. Clearly, we must investigate this issue from other perspectives.

Table 2.1 The 14 GRBs studied by Prochter et al. (2006b).

GRB	z_{GRB}	z_{start}	z_{end}	z_{abs}	W_r(2796 Å)	Δv km s^{-1}
W_r(2796) > 1 Å MgII Statistical Sample						
000926	2.038	0.616	2.0			
010222	1.477	0.430	1.452	0.927	1.00 ± 0.14	74,00
				1.156	2.49 ± 0.08	41,000
011211	2.142	0.359	2.0			
020405	0.695	0.359	0.678	0.472	1.1 ± 0.3	65,000
020813	1.255	0.359	1.232	1.224	1.67 ± 0.02	4,000
021004	2.328	0.359	2.0	1.380	1.81 ± 0.37	97,000
				1.602	1.53 ± 0.37	72,000
030226	1.986	0.359	1.956			
030323	3.372	0.824	1.646			
050505	4.275	1.414	2.0	1.695	1.98	176,000
050730	3.97	1.194	2.0			
050820	2.6147	0.359	1.850	0.692	2.877 ± 0.021	192,000
				1.430	1.222 ± 0.036	113,000
050908	3.35	0.814	2.0	1.548	1.336 ± 0.107	147,000
051111	1.55	0.488	1.524	1.190	1.599 ± 0.007	45,000
060418	1.49	0.359	1.465	0.603	1.251 ± 0.019	124,000
				0.656	1.036 ± 0.012	116,000
				1.107	1.876 ± 0.023	50,000

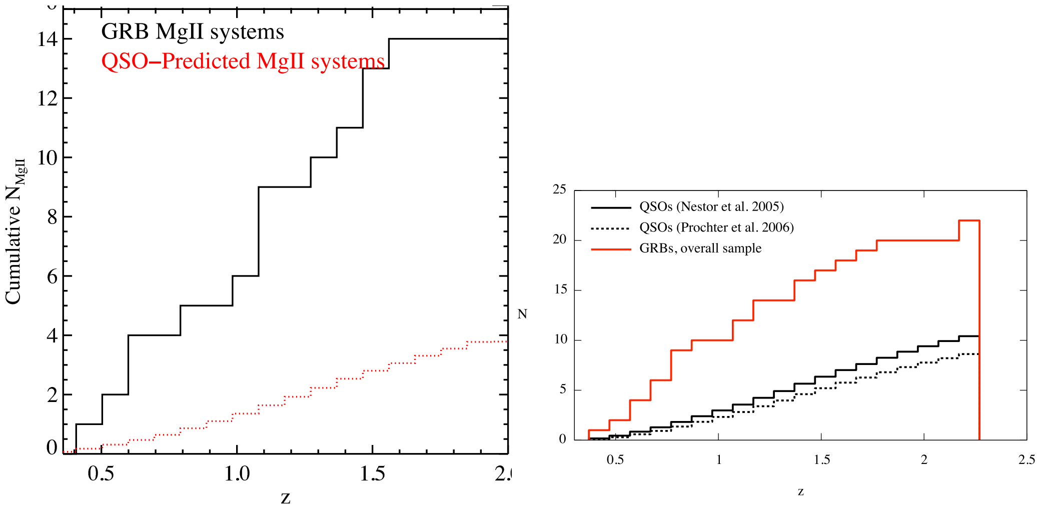

Figure 2.3 The cumulative number density of observed strong intervening MgII absorbers in GRB and quasar sight-lines from Prochter et al. (2006b) **left** Vergani et al. (2009) **right**.

2.1.2 Solutions to the MgII problem: Current research and review

We have shown that the number density of strong intervening MgII absorbers detected in GRB afterglow spectra is significantly higher than those found in similar quasar spectra. This discrepancy does not exist for CIV absorbers, suggesting an influence from sight-line/absorber geometry. Here, we review the most straightforward solutions that have been proposed to solve this discrepancy. Not reviewed are 1. the partial MgII covering factor proposed by Frank et al. (2007), and 2. the possibility that some fraction of MgII systems in GRB afterglow spectra are associated with the GRB. These two explanations have been ruled out definitively since their first postulations (Prochter et al. 2006b; Porciani et al. 2007; Sudilovsky et al. 2007, see e.g.).

Dust Extinction

Light is attenuated as it passes through space containing dust particles. The type (and more specifically, size) of these particles determines the energy dependent attenuation. These dust extinction laws have been studied in great detail for our own Milky Way (MW) and closest neighbors, the Large and Small Magellanic Clouds (LMC,SMC) (Allen 1976; Schlegel et al. 1998; Schlafly & Finkbeiner 2011; Fitzpatrick 1986; Prevot et al. 1984). However, the effects of dust at cosmological distances is extremely difficult to quantify due to the lack of standards with which to compare an object.

Magnitude limited surveys are inherently sensitive to dust. If an object is sufficiently attenuated by dust along the line of sight, the object could be missed in surveys regardless of its intrinsic brightness. The importance of this effect on surveys of quasars is important to understand for this reason. Several studies have been performed to quantify the effect of dust on quasar surveys. Most notably, there are differing conclusions between the Complete Optical and Radio Absorption Line Survey Ellison et al. (2004, CORALS) and European Large-Area ISO Survey (Willott et al. 2004, ELIAS). These surveys have compared optically selected with radio and x-ray selected AGN samples. CORALS shows no evidence of an optical selection effect, while ELIAS finds that many optically faint quasars are affected by dust extinction. Admittedly, small number statistics are likely to play a role in both surveys.

It is intriguing that Ellison et al. (2006) found evidence of large dust depletion in intervening MgII absorbers along GRB 060418. For one of the absorbers, at $z = 1.11$, a 2200 Å bump, typical in the Galactic extinction, was clearly detected for the first time at high redshift. This has yet to be found in QSO spectra.

Measurement of the dust content of intervening absorption line systems has also been studied. The individual dust content of a few absorbers have been measured to correspond to a color excess $E(B-V) \sim 0.1$ (Junkkarinen et al. 2004; Ellison et al. 2006). Vladilo & Péroux (2005); Wild et al. (2006) have found somewhat lower color excesses of $E(B-V) \sim 0.06 - 0.10$ for strong CaII and ZnII systems. York et al. (2006) and Ménard et al. (2008) have found that significant reddening occurs only as $W_{r,Mgii}$ approaches or exceeds ~ 1.5Å.

By building on these previous analysis, we have estimated the extent to which dust extinction is likely to account for the differing GRB/QSO MgII number densities. By using a Monte-Carlo analysis of SDSS quasar sight-lines, we conclude that dust extinction is likely to account for $\sim 10\%$ of this difference in the most optimistic case. The main results of the simulation are presented in Fig. 2.4. For a full analysis, we refer the reader to Sudilovsky et al. (2009). These results are consistent with an independent analysis using data from the Millennium Run performed by (Porciani et al. 2007).

Gravitational lensing

Objects that intersect the line of sight to a background source may increase the observed flux from that source due to gravitational lensing. The galaxies hosting MgII absorbers are obvious candidates for this effect. However, for MgII induced gravitational lensings to account for the MgII issue, its net effect on quasar and GRB afterglow spectroscopy must be different. Borgeest et al. (1991) noticed that quasar samples selected by combining radio and optical measurements contained significantly more lensed sources than samples constructed from detections in a single wavelength regime. Wyithe et al. (2003) formally showed that sources whose flux is uncorrelated in multiple wavelength regimes are more likely to be lensed in such surveys, leading to the so called *multi-band magnification bias*. GRBs make perfect candidates to be affected by a multi-band magnification bias, as their γ and optical fluxes are uncorrelated (Nardini et al. 2006). Porciani et al. (2007) suggest that up to 30% of *Swift* GRBs could be micro-lensed, making optical spectra easier to take. Micro-lensing could also give rise to time variability, following a scenario similar to the one considered byLewis & Ibata

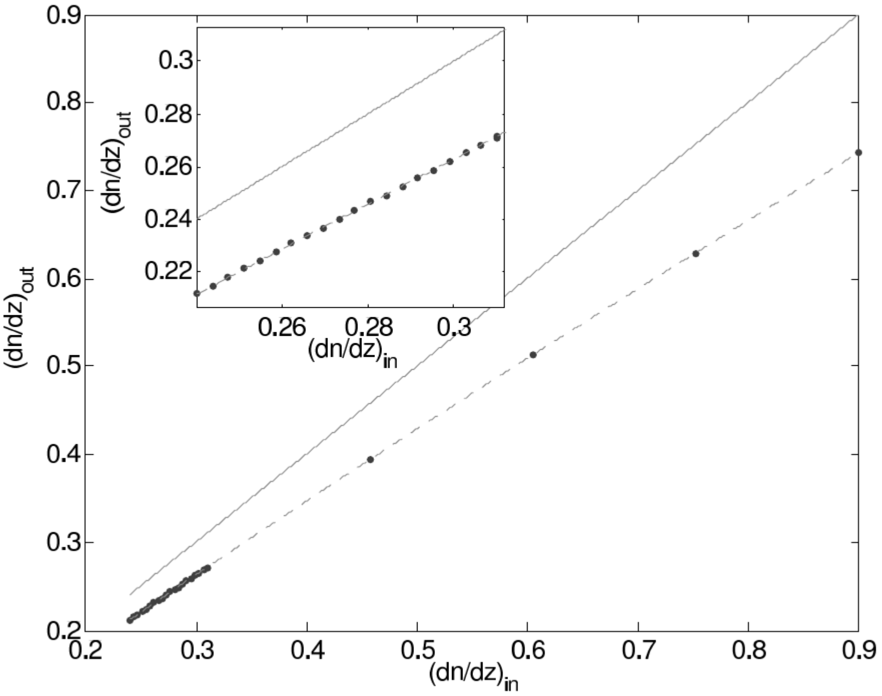

Figure 2.4 Simulated output MgII number density as a function of input MgII number density after accounting for the dust introduced from the absorbers along the line of sight. Based on our current understanding of the dust hosted by MgII absorption systems, the difference between input and output is on order 10%. Adapted from Sudilovsky et al. (2009).

(2003).

However, recent investigations of lensing in GRB afterglows has showed no evidence of any significant contribution from such a bias. Ménard et al. (2008) compared a sample of SDSS quasars with strong MgII absorbers to a sample of SDSS without absorbers and found no significant difference in their redshift or mean magnitude distributions. Rapoport et al. (2012) predicted the lensing characteristics of three GRBs that were thought to be strong candidates for lensing, and found no evidence of lensing in follow-up observations (Rapoport et al. 2013).

These recent studies show that gravitational lensing likely does not play a significant role in the MgII problem.

Absorbers associated with the GRB host environment

It is generally accepted that metals that are ejected at semi-relativistic speeds from QSO or GRB sources would have distinctively broad profiles. These features can be found in QSOs up to $\Delta v \approx 50,000$ km s^{-1} away from the source, and are known as Broad Absorption lines (BALs; Hamann et al. (1993)). However, there has been no evidence that suggests that the same process occurs in GRBs. In fact, BALs are mostly detected in high-ionization absorption lines, which are naturally expected for gas clouds very close to a very luminous source. Therefore, if it is detected for MgII absorbers, it should be even stronger for CIV . Moreover, as relativistic speeds are expected, the absorptions features should be very large in the velocity space. This is clearly seen in BALs, but not at all present in normal intervening MgII or CIV absorbers.

The scenario proposed by Porciani et al. (2007), where a supernova remnant associated with the GRB and its environment, with multiple high velocity MgII 'clouds', would give a MgII number excess is not supported by our results. It is true that this effect might be less significant in CIV absorbers, because the intrinsic number density of intervening systems is large and the contamination can only be small. Whereas, there are generally few MgII absorption systems per sight-line, this misidentification can significantly affect statistics. This scenario must only occur once or twice among the MgII 14 GRB sample to significantly affect results. However, such high-velocity absorbers would require velocities of the gas of half the speed of light to be misidentified as an 'intervening absorber'. This is not typically observed in SN remnants. Intrinsic broadening of the absorbing features is also expected to be much larger than those observed.

Chapter 3

Instrumentation

3.1 UVES

The Ultraviolet and Visual Echelle Spectrograph (UVES) is an ESO built and operated high resolution optical spectrograph that is used on the VLT (Dekker et al. 2000). UVES has a red and blue arm, whose measured efficiency is presented in Fig. 3.1. The instrument has two dichroic mirrors, each optimized for red or blue wavelengths. An observer may choose to use the dichroics to optimize exposure time towards a certain wavelength regime. An iodine cell may be introduced into the system to provide a precise wavelength with which to calibrate against, which in practice is useful for measurements of radial velocities of a few tens of km s^{-1}. UVES offers extremely high resolution, which enables the measurement of sub-structures in metal absorption line systems, given that the background source provides high enough S/N. A summary of UVES's capabilities are presented in Table 3.1

UVES comes with an image slicer, which enables the spectroscopic slit to be subdivided, potentially leading to a higher S/N of spectral features by sampling smaller areas of the object in question. The use of the image slicer is a trade-off between having spectral features less smeared across a larger slit, and the reduced overall flux from using an effectively smaller slit.

Table 3.1 Instrumental characteristics per operating mode for UVES.

Mode	Accessible range [nm]	Max Resolution [nm]	Covered range [nm]	Limits [mag$_{\mathrm{AB}}$]
Blue arm	300-500	80,000	80	17-18
Red arm	420-1100	110,000	200-400	18-19
Dichroic #1 (blue)	300-400	80,000	80	17-18
Dichroic #1 (red)	500-1100	110,000	200	18-19
Dichroic #2 (blue)	300-500	80,000	80	17-18
Dichroic #2 (red)	600-1100	110,000	400	18-19
Iodine cell	500-600	110,000	200	17

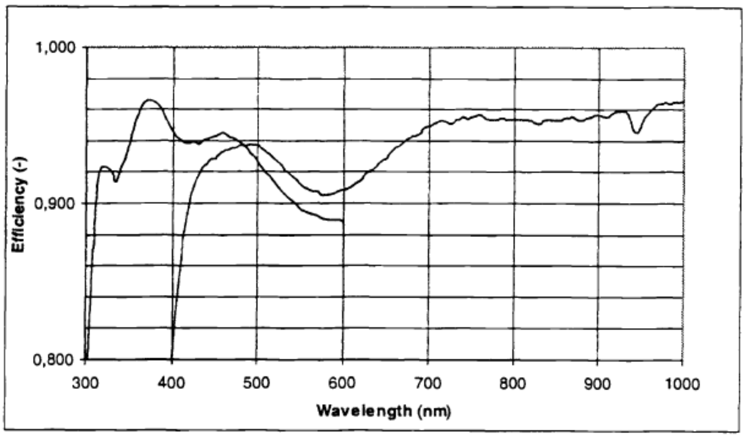

Figure 3.1 Measured efficiency for UVES red and blue arm, adapted from Dekker et al. (2000).

Raw UVES data are reduced by a data reduction pipeline provided by ESO, which provides a wavelength calibrated 2-D spectra. Normalization is done by fitting and dividing by the continuum flux. Data whose proprietary period have passed are provided by the ESO data archive[1].

3.2 IRAC

The InfraRed Array Camera (IRAC) is a focal plane instrument on the Spitzer Space Telescope (Fazio et al. 2004). The instrument is a CCD that provides $5.2' \times 5.2'$ images in four bandpasses centered at 3.6, 4.5, 5.8, and 8.0 micrometers. The four channels, dubbed channel 1-4 respectively, image slightly offset field of views simultaneously. The filters that IRAC uses are presented in fig3.2. Channels 1-2 and channels 3-4 image two fields $6.5'$ apart, with a $1.5'$ gap between them. Each CCD is 256×256 pixels, corresponding to a pixel size of 1.2 square arcseconds. The image quality characteristics are presented in Table 3.2.

On may 15, 2009 Spitzer depleted its cryogen supply under expected conditions. This marked the start of the Spitzer Warm Mission, which for IRAC meant the effective decommissioning of IRAC channels 3-4, and a slightly reduced sensitivity of channels 1-2. Despite this onset, the NIR imaging capabilities in the remaining two bandpasses still remain extremely high, easily reaching sensitivities of a few micro-Jansky.

Since IRAC is mounted on a space based observatory, the quickly varying sky NIR background does not require IRAC to take many short exposures to perform adequate background subtraction. In IRAC's case, the NIR background consists of zodiacal light, ISM, and cosmic background radiation, while zodiacal light is the most dominant of

---

[1] http://archive.eso.org

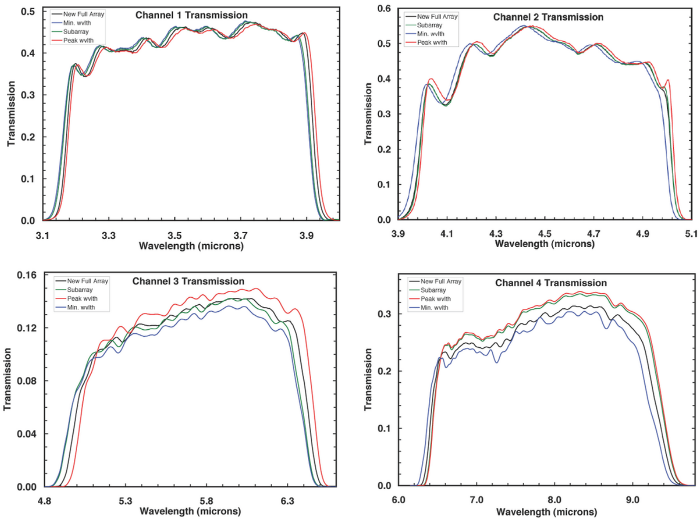

Figure 3.2 Filter transmission curves for IRAC channels 1-4. The mean wavelengths are 3.5, 4.5, 5.8, and 8.0 micrometers, respectively.

Table 3.2 Image quality characteristics of IRAC. Noise pixels is the equivalent number of pixels whose noise contributes to a linear least-squares extraction of the flux of a point source. The FWHM and FWHM of PRF are the average measurements of 25 stellar FWHMs, and the measurements of those stellar FWHMs whose center fell into the center of a pixel, respectively.

Channel	Noise pixels	FWHM (arcsec)	FWHM of PRF (arcsec)	Pixel Size (arcsec)
1	7.0	1.66	1.44	1.221
2	7.2	1.72	1.43	1.213
3	10.8	1.88	1.49	1.222
4	13.4	1.98	1.71	1.220

these sources. This fact, combined with the rather large PSF and pixel size, mean that IRAC is most limited by the confusion limit[2] instead of sensitivity.

Spitzer data are automatically reduced, astrometrized, and calibrated by a NASA data reduction pipeline. These data whose proprietary period have passed are available through the Spitzer Heritage Archive[3].

3.3 GROND

The Gamma-ray Optical and Near-infrared Detector (Greiner et al. 2008, GROND) is designed to quickly discover and measure the photometric redshift of GRB afterglows using the Lyman-α dropout technique (see e.g. Krühler et al. 2011, and references therein). To this end, the detector images seven bandpasses between the range of 380 nm to 2400 nm simultaneously. The filters are based on the Sloan $g'r'i'z'$ and 2MASS JHK_s standards (see Fig. 3.3). GROND is mounted on the 2.2m MPG Ritchet-Cretien telescope in La Silla Observatory, Chile and has been operational since late 2007. GROND shares the telescope with two other permanently mounted instruments.

As part of the installation of GROND, we have installed a movable mirror (M3) that enables the rapid (< 1 minute) changing of active instrument by modifying the location of the focal plane inside of the telescope. This feature allows rapid response mode (RRM) functionality, resulting in a typical time between a GRB trigger and GROND exposure of a few minutes assuming target visibility, even if another instrument was observing immediately prior. This fast response, coupled with the simultaneous nature of GROND exposures in seven filters, has resulted in the final result that the GROND is responsible for the most complete and unbiased sample of GRB afterglows to date (See discussion in §2).

Because GROND images simultaneously in the optical and NIR, special care must be taken to optimize the quality of observations. All observations follow a square dither pattern that are eventually combined with sub-pixel accuracy based on object position correlation. To account for the highly variable NIR sky background, exposures are always read-out in 10s intervals. A further fine-grained dither pattern is executed per telescope dither position in the K_s band by using a dedicated flip mirror internally in the GROND vessel.

GROND is capable of RRM observations with a typical Δt between trigger and exposure of a few minutes. The majority of this time is taken by dome slew. Since no photometric properties of a new trigger can be reliably estimated in this time-frame, we use an observational strategy that maximizes the probability of detecting a counterpart as quickly as possible, since effects of late time central engine activity, reverse shocks, and effects from the immediate circumburst environment are expected to affect afterglow emission only at early times. To this end, we observe with ~ 1 minute dithered exposures of the field, increasing progressively over the next hour to ~ 6 minute dithered

---

[2] The limit at which one can no longer resolve a source from background

[3] http://sha.ipac.caltech.edu/applications/Spitzer/SHA/

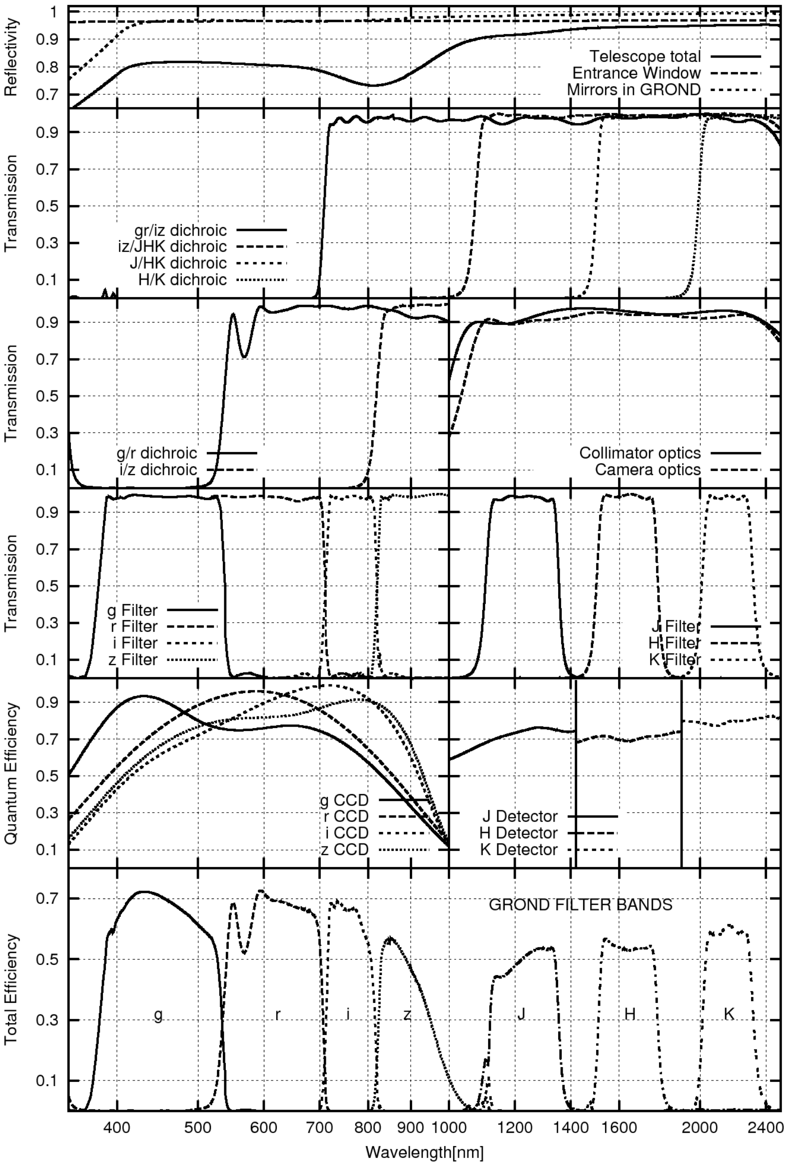

Figure 3.3 GROND filter characteristics and photon efficiency. From top to bottom: Telescope and mirror reflectivity, dichroics transmission, filter transmission, quantum efficiency, and total integrated efficiency. The difference between Sloan and GROND in $g'r'i'z'$ is negligble. The filters were chosen to measure the absorption due to intergalactic Lyman-α and thus the photometric redshift from redshifts GRB afterglows between $3 \lesssim z \lesssim 10$. Adapted from Greiner et al. (2008).

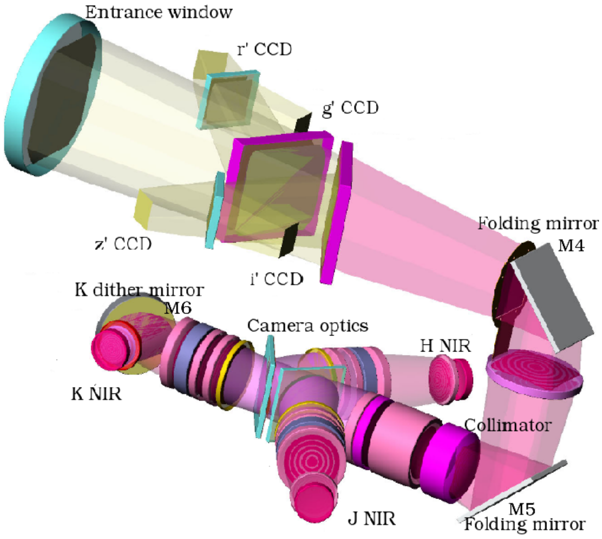

Figure 3.4 Interior schematic view of the GROND vessel. Light passing through the entrance window is routed by dichroic mirrors to their respective CCDs. The field of view of the optical channels is $5.4' \times 5.4'$, while the NIR field of view is enlarged by a focal reduced to $10' \times 10'$. Adapted from Greiner et al. (2008).

exposures. This strategy is manually modified as needed, depending on the properties of the afterglow.

Data are processed using a custom built reduction and analysis pipeline. The pipeline uses the Image Reduction and Analysis Facility (IRAF[4]) to perform standard image reduction tasks including, including the separation of images per band, bias and flatfielding, background subtraction, stacking, and distortion correction. After a reduced image is produced, an astrometric solution is calculated by matching sources extracted with SExtractor with catalogs from USNO-B1 (Monet et al. 2003) or SDSS (Adelman-McCarthy et al. 2008) in the case of optical, and 2MASS (Skrutskie et al. 2006) in the case of NIR. Astrometric accuracy produced by our pipeline is on order $0.2''$ in the optical and $0.3''$ in the NIR. Photometric accuracy is limited to the calibration catalog, which is typically 0.05 mag in the case of the SDSS and 0.1 mag in the case of 2MASS. USNO-1B is never used as a photometric catalog for this reason – instead, the optical magnitudes derived from instrumental zeropoints, which are monitored and updated based on SDSS standard fields on a monthly basis, are preferred. The RMS scatter of these “2nd-order” SDSS calibrated zeropoints is on order 0.1 mag.

---

[4] IRAF is distributed by the National Optical Astronomy Observatories, which are operated by the Association of Universities for Research in Astronomy, Inc., under cooperative agreement with the National Science Foundation.

Chapter 4

C IV absorbers in GRB afterglows[1]

4.1 The Data

4.1.1 The GRB sample

GRB optical afterglow spectra of 5 GRBs were taken using the high resolution spectrograph UVES. These are: GRB 050730 at $z = 3.967$ (Chen et al. 2005; D'Elia et al. 2007), GRB 050820 at $z = 2.612$ (Ledoux et al. 2005; Prochaska et al. 2005), GRB 050922C at $z = 2.198$ (Jakobsson et al. 2005; Piranomonte et al. 2006), GRB 060418 at $z = 1.489$ (Dupree et al. 2006; Vreeswijk et al. 2007), and GRB 060607 at $z = 3.082$ (Ledoux et al. 2006). The spectra were normalized by fitting a polynomial function to the continuum. The spectra of GRBs 050820, 050922C, and 060607 were used for the C IV sample with a total absorption path-length of $\Delta z = 2.25$ and a mean redshift of $\langle z \rangle = 2.63$. The two other GRB spectra – GRB 060418, 050730 – were excluded from the sample, due to lack of C IV redshift coverage and poor S/N. For the Mg II analysis, we used all these spectra, as the EWs are robust measurements when the S/N is not very high. The spectra used in the C IV survey all have high S/N and resolution (Table 4.1 and Fig. 4.1).

4.1.2 The QSO sample

Our QSO sample comes from a larger sample of quasars used by Boksenberg et al. (2003). We use their identification of C IV systems and column densities, and we derived cumulative numbers and column density distribution from their tables. The resolution and redshift range of the QSO sample is very similar to the GRB sample. However, the S/N is significantly higher in the QSO sample (Table 4.1).

The QSO C IV sample has a very similar Δz and $\langle z \rangle$ of 2.26 and 2.65, respectively. A total of 20 C IV systems were identified in the GRB sample, and a total of 40 systems in the QSO sample. The factor of two difference in the number of systems is due to the

---

[1] Published in Sudilovsky et al. (2007)

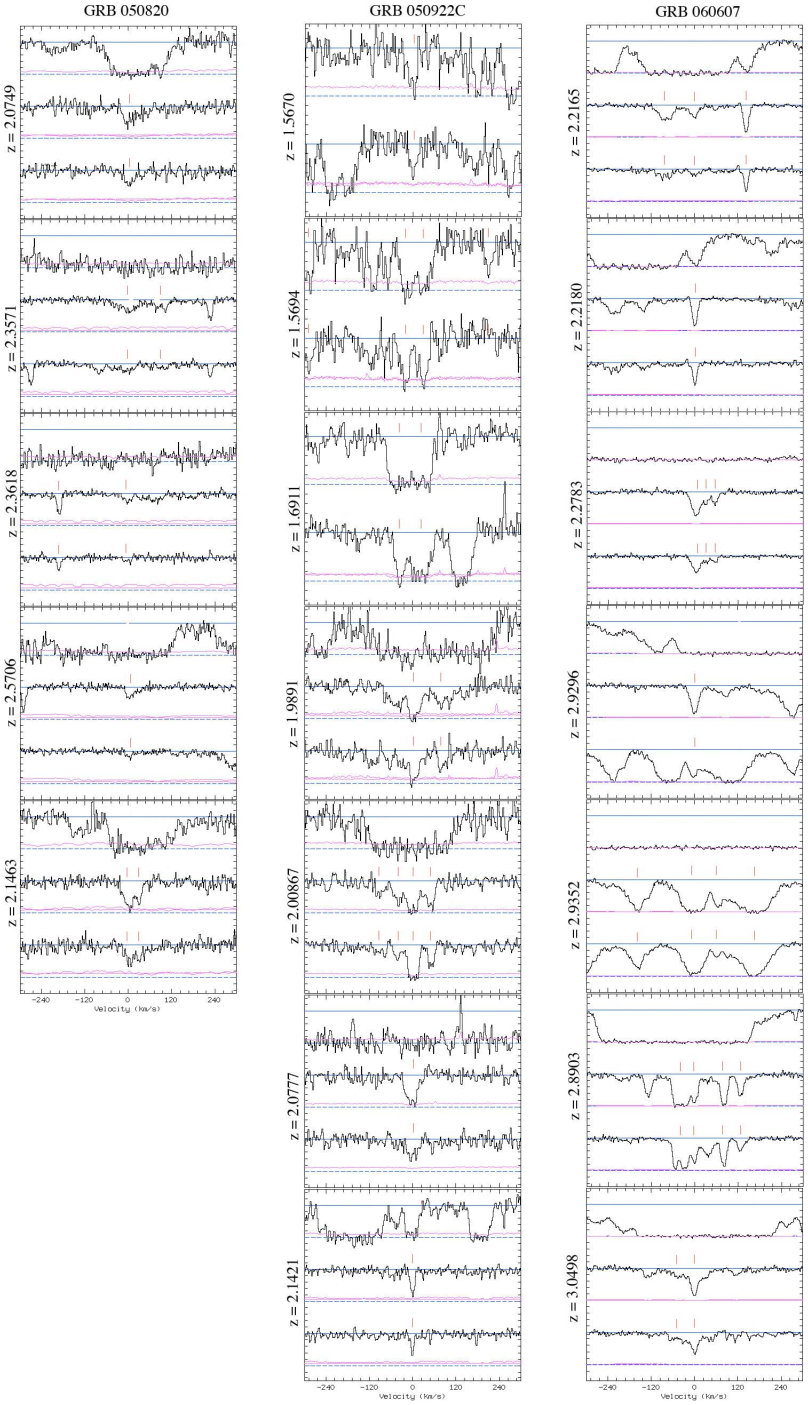

Figure 4.1 Normalized flux vs Velocity profiles for CIV systems in the three GRBs studied. From left to right are GRB 050820, GRB 050922C, and GRB 060607. The pink line represents the associated error spectra. The panels, from top to bottom, plot Ly-α (when applicable), CIV 1548, and CIV 1550.

Table 4.1 Sample Characteristics

Source	z_{em}	$z_{min} - z_{max}$	No. C IV systems	FWHM (km s^{-1})	S/N[a]
GRB 050820	2.612	1.836-2.582	5	6.3	6 – 18 –18
GRB 050922C	2.198	1.511-2.168	7	6.8	7– 12 – 12
GRB 060607	3.082	2.205-3.052	7	6.9	58 – n/a – 61
Q1626+6433	2.320	1.607-2.290	15	6.6	88 – 128 – 137
Q1442+2931	2.661	1.875-2.631	14	6.6	113 – 107 – 121
Q1107+4847	2.966	2.114-2.936	11	6.6	90 – 94 – 81

[a] S/N over three pixels outside the Lyman forest sampled near the three wavelengths $\lambda\lambda\lambda$1270,1380,1500 in the rest frame of the GRB or QSO.

higher S/N and thus lower detection limits of the QSO sample. Information specific to particular GRBs or QSOs are found in Table 4.1.

The software ESO-MIDAS and the context FITLYMAN were used to derive the column density, N, by simultaneously fitting Voigt profiles to both lines of the C IV doublet. If a system contained multiple components, the column density used was the sum of the column densities of the components.

4.1.3 C IV Selection techniques

The C IV systems usually are well defined and have multiple absorption features with a velocity distribution structure of up to a few hundred km s^{-1} (Ellison 2000; Boksenberg et al. 2003; Songaila 2005, 2006). One or more C IV 'cloudlets' can compose a C IV system. Individual systems (i.e., belonging to one physical entity such as a galaxy) are usually separated from each other by more than a few hundred km s^{-1}, and are often associated with Ly-α absorption. In two cases, several C IV absorption features that share the same Ly-α absorption, were classified as two distinct systems. All other C IV absorption features associated with distinct Ly-α absorption are considered individual systems. The velocity spread of these C IV absorption features would have been in excess of 600 km s^{-1} if classified as one system. The column density of the C IV system is the sum of the column densities of all of its constituent 'cloudlets'. Velocity profiles of all identified systems are found in Fig. 4.1. Table 4.2 presents the redshift, column density $N_{\rm CIV}$, and Doppler parameter b of all C IV systems detected in the GRB sample

In this study, only C IV *systems* outside of the Lyman-α forest (i.e., $z \geq 1215.67 \times (1 + z_{em})/1548.1949 - 1$) are included in the sample. No systems within $\Delta v = 2300$ km s^{-1} (corresponding to a physical separation of 5.5 Mpc at $z = 2.3$) of the redshift of the GRB of QSO were included to prevent any unknown differential effects between the GRB and QSO host environment. A total of 3 C IV systems were excluded from the

Table 4.2 C IV Systems

	System	$z_{\rm abs}$	$\log N_{CIV}$ $[cm^{-2}]$	b (km s^{-1})
GRB 050820				
	1	2.0749	13.64	22.1
	2	2.1463	13.43	23.3
			13.33	6.1
	3	2.3571	13.43	23.3
			12.83	6.5
			13.21	5.9
	4	2.3618	13.05	17.4
	5	2.5706	13.12	14.5
GRB 050922C				
	1	1.5670	13.78	14.7
	2	1.5694	14.20	14.1
			14.20	18.2
	3	1.6911	14.44	25.3
			14.61	20.9
	4	1.9891	14.26	13.1
			13.55	12.7
	5	2.0087	13.60	15.7
			17.20[a]	5.6
			13.73	11.3
	6	2.0778	13.89	17.9
	7	2.1421	13.47	5.1
GRB 060607				
	1	2.2165	13.59	28.4
			13.21	15.5
	2	2.2180	13.55	6.6
	3	2.2783	13.64	13.8
			12.95	8.2
			13.01	8.6
	4	2.8903	14.12	5.6
			14.27	11.7
			13.75	7.8
			13.95	8.0
			13.42	9.8
	5	2.9296	13.71	12.0
	6	2.9352	14.14	27.4
			14.54	28.8
			14.68	35.7
	7	3.0498	13.19	20.2
			13.70	11.1

[a] Heavily saturated.

QSO sample, and 1 system from the GRB sample.

4.1.4 Completeness limit

Since the S/N in the spectra vary, we derived the lowest detection limit in our GRB sample. A completeness limit of 1 Å rest equivalent width ($W_r \geq 1$ Å) was used by P06 for the MgII sample. In this study, column density is used as the parameter to determine completeness. A theoretical rest equivalent width limit of 3 σ is derived from the various error spectra for the weaker line of the doublet (CIV λ1550). Since the ratio of the stronger to the weaker line is 2:1, for small absorptions (i.e. in the linear part of the curve of growth), this corresponds to a detection limit of 6 σ for the stronger line (CIV λ1548). When combined with the fact that CIV systems are identified by the presence of *both* of these lines, our CIV detection limit is conservative and is $> 6\sigma$.

This value is converted to a column density limit for a given Doppler parameter b, from the linear portion of the empirical curve of growth of CIV . The final column density limit for the survey is the maximum column density limit among the 6 spectra of the 3 GRBs (Fig. 4.2). Limits were calculated using $b = [5, 10, 15]$ km s^{-1} (colored lines from bottom to top in Fig. 4.2). We notice that the mean Doppler parameter in the sample is $\langle b \rangle = 14.5$ km s^{-1}, and that large b values are typically associated with large CIV column density, which are easy to detect.

As our S/N does not vary much for $z < 2.3$, and for $z > 2.3$ (apart from a couple of two small redshift bins) we have chosen for the final analysis, a conservative limit close to the $b = 15$ km s^{-1} line, described by a step function, with $N_{lim} = 10^{13}$ cm^{-2} and $N_{lim} = 10^{12.7}$ cm^{-2}, in the lower and higher redshift bin, respectively (dashed line in Fig. 4.2). As the average resolutions of the GRB and QSO spectra are within 5% of each other and are all well above the value to resolve the CIV doublet, it is not necessary to compensate for different resolutions when comparing the different spectra (Table 4.1).

The black and the pink points in Fig. 4.2 represent the measured GRB CIV and QSO CIV column densities, respectively.

4.2 Methods

4.2.1 Mg II absorbers in the GRB sight-lines

To verify if the over-density of MgII systems along GRB sight-lines is not due to the inhomogeneity of P06's sample, we have performed the same analysis on our homogeneous sample of UVES spectra using *exactly* the same search criteria. We notice that two UVES afterglow sight-lines are not in the P06's sample: GRB 050922C and GRB 060607. Table 4.3 shows the GRB sight-lines used, the starting and ending redshift of the potential MgII system, the redshifts of the identified MgII systems, and the rest-frame equivalent width that we measured.

The total redshift path covered by the UVES sample is dz=6.75 with a mean redshift of $\langle z \rangle = 1.3$. We find 6 MgII systems with a rest-frame equivalent width larger than

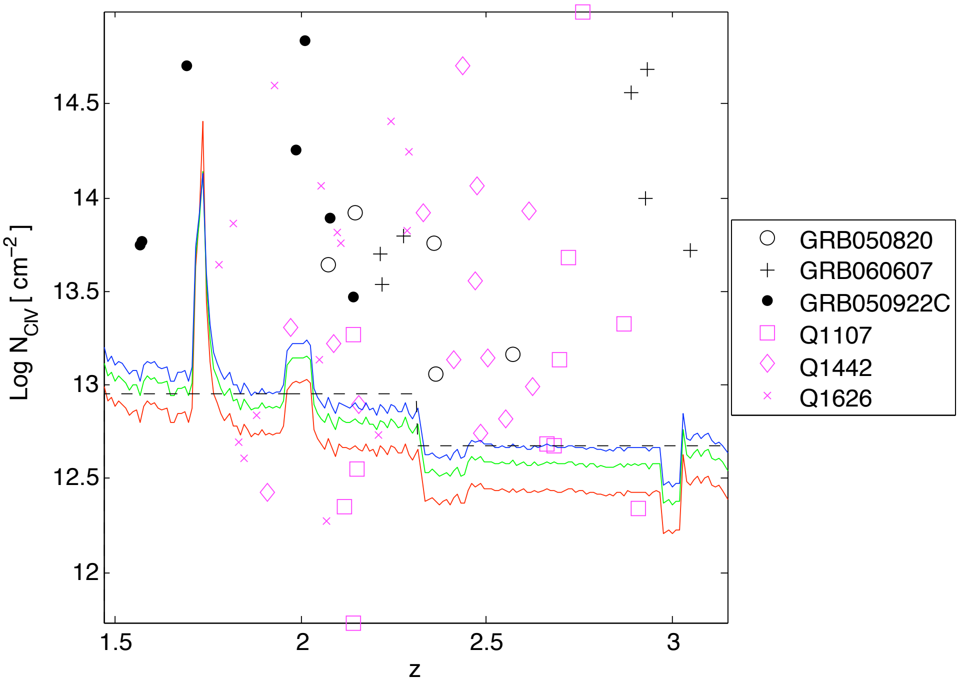

Figure 4.2 Column density of CIV systems, measured in GRB (black points) and QSO (pink points) sight-lines, respectively, as a function of redshift. The lines represent the completeness limit to detect lines at $> 6\sigma$ confidence level. From the bottom to top, the limits for $b = [5, 10, 15]$ km s^{-1} are plotted. The flat dashed line represents the limit used in this study.

Table 4.3 Identified MgII systems in the UVES sample

GRB	z_{GRB}	z_{start}	z_{end}	z_{abs}	$W_r(2796\ \mathring{A})$[a]
050730	3.9686	1.160	2.0	1.7734	0.913 ± 0.008
050820	2.6145	0.572	2.0	0.6915	2.896 ± 0.017
				1.4288	1.329 ± 0.022
				1.6204	0.238 ± 0.009
050922C	2.1991	0.391	2.0	0.6369	0.167 ± 0.009
				1.1068	0.589 ± 0.024
060418	1.4900	0.359	2.0	0.6026	1.257 ± 0.008
				0.6558	1.071 ± 0.008
				1.1069	1.836 ± 0.006
060607	3.0748	0.772	2.0	1.5103	0.199 ± 0.006
				1.8033	1.906 ± 0.008

[a] The error on the equivalent width is calculated from the noise spectrum; an error on the continuum normalization has not been included.

unity. This corresponds to a number density $dn/dz = 0.89 \pm 0.36$, consistent with the $dn/dz = 0.90 \pm 0.24$ found by P06, at a mean redshift $\langle z \rangle = 1.1$.

Although our redshift path is smaller than that of P06, our sample of UVES spectra is homogeneous and of much higher quality, and provides a preliminary confirmation of the MgII excess observed in GRB sight-lines. As the sample will grow, a more sophisticated analysis will be possible, such as the one we present in the following sections on the CIV systems.

4.2.2 Cumulative number of CIV systems vs z

The cumulative number of CIV systems as a function of redshift is shown in Fig. 4.3 for the QSO and GRB samples. A bin size of $z = 0.25$ was used and error bars were calculated assuming a Poisson distribution, where $\sigma \propto \sqrt{n}$, with n the number of CIV systems. In addition to providing an easy visual comparison with the results obtained by P06 , this method has the potential to amplify systematic differences in the number of CIV systems that are too small to notice on a redshift bin by bin basis.

Fig. 4.3 shows no significant difference between the GRB and QSO samples. The detection limit discussed in §4.1.4 was applied to both the GRB and QSO subsamples. To demonstrate that an excess of ~ 4 times detected in MgII systems would be easily detected in our CIV study, we multiply by four the cumulative number of CIV systems measured in the GRB sample (plotted as crosses in Fig. 4.3).

In addition, the data were split into two subsamples based on column densities, for $N_{CIV} > 10^{13.8}$ cm^{-2} and $N_{CIV} \leq 10^{13.8}$ cm^{-2}. This corresponds to the median column density of the full CIV sample. Though we mentioned that there has not been

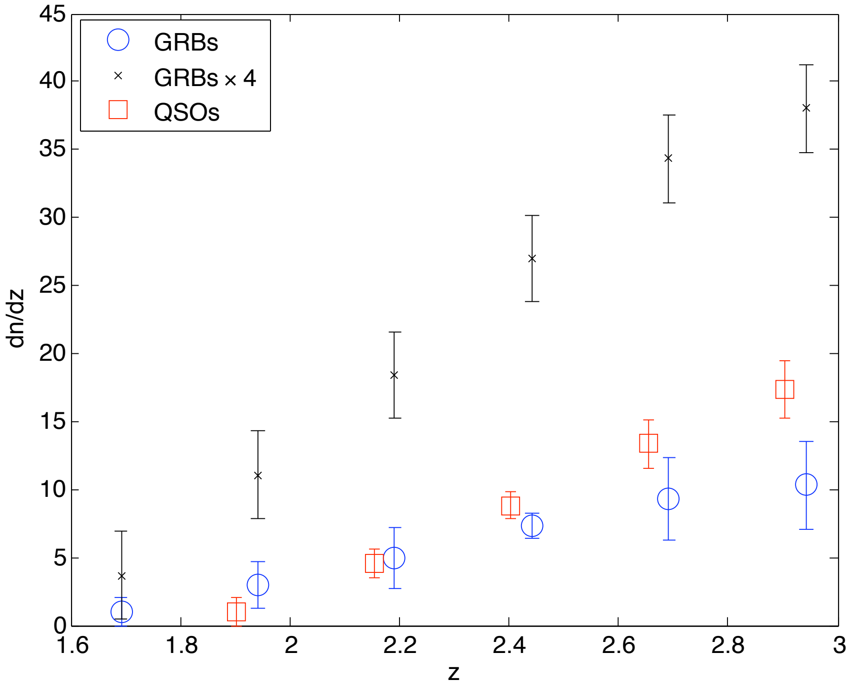

Figure 4.3 Cumulative number of CIV systems in GRB (open circles) and QSO (open squares) sigthlines, per redshift bin of $\Delta z = 0.25$, as a function of redshift. The data designated as GRBs × 4 (crosses) represents an incidence of 4 times as many CIV systems as were actually measured.

a relationship established between CIV and MgII systems, we split the sample to test if there is any difference in CIV systems based on their absorption strength. Again, there is no detectable difference in the number density of CIV systems for GRB or QSO sight-lines, although small number statistics play a more significant role for the subsamples than in the full sample.

4.2.3 Column Density Distribution

The number of CIV systems per column density interval and absorption path-length $d^2n/dNdX$, in GRBs is compared with the same function derived from QSOs. The absorption path-length is defined as:

$$dX = \frac{1+z}{\sqrt{\Omega_M(1+z)+\Omega_\Lambda/(1+z)^2}}dz \ . \tag{4.1}$$

We selected a column density interval of $dN = 10^{0.3}$ cm^{-2}, while $z \equiv \langle z \rangle = 2.37$, corresponds to the mean redshift of the sample. The redshift bin dz is the total redshift interval covered by all sources, from z_{min} to z_{max}, as described in §4.1.3.

Using the column density distribution to compare the incidence of CIV systems allows one to account for multiple redshift coverage as well as compare systems in spectra with different S/N, without discarding any data due to different completeness limits. In addition, the column density distribution provides an easy comparison of the incidence of strong and weak absorbers alike in different lines of sight.

In Fig. 4.4 we show the results. The sample completeness is demonstrated by the flattening of the power-law distribution, which happens at $\log N_{\rm CIV} = 13.6$ and $\log N_{\rm CIV} = 12.6$, for the GRB and QSO samples, respectively. The two column density distributions above these limits are best fit with a power-law of the form $dn/dN \propto N^{-\beta}$, where $\beta = 1.5 \pm 0.2$ for the QSOs, and $\beta = 1.2 \pm 0.5$ for the GRBs.

As in the case of the cumulative number, the CIV column density distributions in GRB and QSO sight-lines are consistent. We also show that an excess of ×4 would show a clear deviation of the two distributions.

4.3 Results

We have studied the statistical difference between intervening absorbers in GRB and QSO sight-lines. Our MgII sample confirms the overdensity detected by P06 in GRB sight-lines. On the other hand, there is no statistical difference in the number of CIV systems, considering both the cumulative number and the column density distribution. MgII and CIV do not behave the same way. We consider the effects of dust extinction, gravitational lensing, and absorbers associated with the circumburst environment in the following subsections. We note that the redshift intervals covered by the CIV and MgII absorbers are different, $1.6 < z < 3.1$ for the former and $0.5 < z < 2$ for the latter.

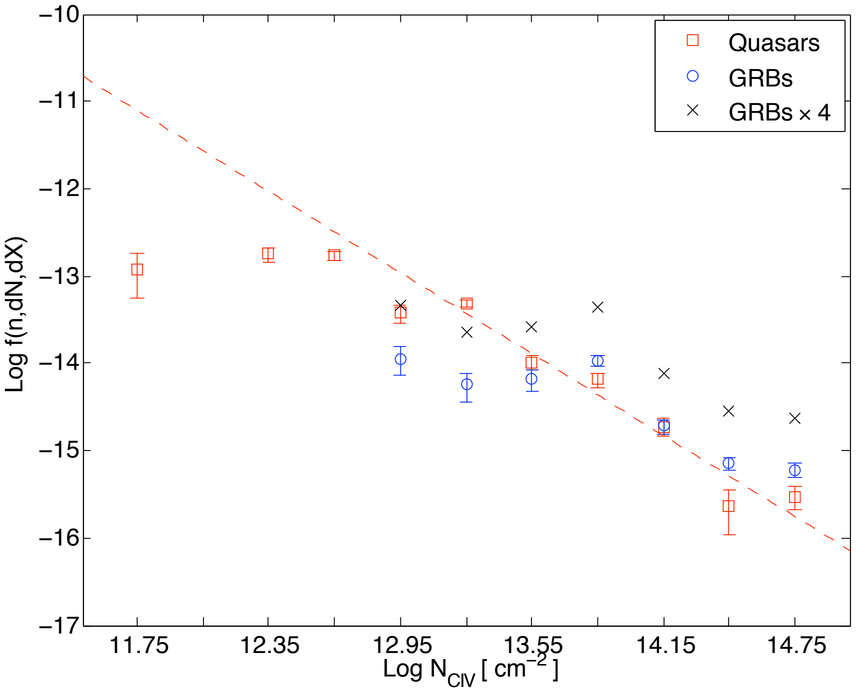

Figure 4.4 Column density distribution of the GRB (open circles) and QSO (open squares) samples. Plotted in black crosses is the column density distribution of 4 times as many C IV systems than there actually were. The data are best fit by a line with a slope of [-1.5±0.2, -1.2±0.5] and offset of [6±3, 3±6] for the QSO and GRB sample, respectively. The best fit for the QSO sample is plotted as a dashed line.

4.4 Summary

An excess of MgII intervening absorbers along high-z GRB sight-lines relative to similar absorbers found in high-z QSO spectra was recently found. These MgII absorbers trace galaxies intersecting bright background point sources. The total number of absorbers in GRB sight-lines is nearly 4 times higher, in the interval $0.5 < z < 2$ (Prochter et al. 2006b).

We have performed a similar study using an additional sample of MgII absorbers, and confirm the previous results. We additionally investigate intervening CIV absorbers and adopted a more detailed analysis. We have compared the number density and column density distribution in 3 GRB sight-lines at $1.6 < z < 3.1$ with the same quantities in QSO sight-lines in a similar redshift interval. There is no detectable difference in the incidence of CIV systems in the two samples, contrary to what found for MgII .

Observationally, the main differences between the CIV and MgII absorbers are the larger impact parameter, the lesser dust extinction, the higher ionization level, the higher redshift, and the larger number density dn/dz of the former with respect to the latter sample. We expect one or more of these factors to be directly or indirectly responsible for the discrepancy.

We exclude the possibilities that some of the intervening MgII or CIV absorbers are intrinsically associated with the GRBs, or that these absorbers have a partial covering factor in QSO spectra. We have shown that the scenario in which statistics being affected through the misidentification of intrinsic systems as intervening systems is unlikely, especially in a survey of CIV absorbers.

Out of the possible effects, dust extinction could cause part of the difference in MgII absorbers. This is due to the fact that QSO studies are generally performed on the bright population, whereas GRBs are primarily selected because of their gamma-ray signal. However, we have shown that dust gives a sizable effect only for the strong MgII absorbers, those with $W_r > 1.5$ Å, which is half of the total sample used by P06. This is true for normal dust, however, with a dust-to-metals ratio similar to the Milky Way. If the dust-to-metals ratio is larger that what was previously thought for at least a fraction of high-z galaxies, the effects of dust extinction would become more pronounced.

In the future, better statistics both for CIV and MgII absorbers in GRB spectra will help to solve the issue. FeII absorbers could be used to probe the same galaxy regions as MgII absorbers. The advantages of using FeII are its larger redshift range (for a higher number statistics), and its less complicated access to column density. The column density is a more meaningful parameter than the equivalent width, used for MgII . A further test is to study the mean Lyα absorption in the diffuse IGM, which is well studied from QSO spectra, and relatively easy to measure in GRB spectra, provided that statistical methods are used, such as the IGM optical method (Fan et al. 2006).

GRB afterglow studies have already demonstrated that there is a population of absorbers, identified as GRB-DLAs and intrinsic to the GRB host, that were very hard to detect before and that show on average very strong absorption features (Savaglio et al.

2003; Berger et al. 2006; Fynbo et al. 2006). It is not known whether the existence of this population is intrinsic to the GRB itself or common in the high-z universe. The study of intervening absorbers presented in this work may show that GRBs are probing the high-z universe better than QSO studies, regardless of the nature of the GRB itself. The results of our work are not conclusive, but they do imply that there may be fundamental assumptions about the structure of the universe and our methods to probe it that need to be reconsidered.

Chapter 5

Clustering analysis of GRB afterglows[1]

5.1 Introduction

Objects near the line of sight to a GRB afterglow are unaffected by light from the event after the afterglow has faded, allowing detailed follow-up of the field to extremely high angular resolutions. The study of sources near quasars are reliant on either extremely high resolution imaging on intrinsically dim quasars, Lyman-α imaging, or very low redshift quasars. Galaxies that give rise to absorption line systems in GRB afterglow spectra have been directly imaged and studied, although the number of robust associations is still extremely small. Chen et al. (2009) find that additional galaxies are found at very close angular distances to GRB host galaxies whose afterglows exhibited strong MgII absorption, though it is unclear what fraction were associated with the absorption line systems. Schulze et al. (2012) proposed galaxy counterpart candidates to absorbers, and additionally found field galaxies with the same redshift as absorption line systems at distances of 130-161 kpc away from the sight-line. The frequency of field galaxies that are associated with MgII absorption line systems is still unclear. However, Lopez et al. (2008) have shown that strong MgII absorbers are strongly associated with galaxy clusters, and that the number density of strong MgII absorbers around galaxy clusters is much higher than those around field galaxies. In this work, we test for any anomalous signatures of field galaxy clustering in GRB and quasar lines of sight.

If there is indeed a higher probability of detecting strong MgII absorption line systems in GRB afterglow than in quasar sight-lines, one should also expect to detect more galaxies at close angular separations to GRB sight-lines. The two point correlation function is a powerful tool to determine if objects are clustered, and, if so, what their correlation lengths are. The angular two point correlation function is formally defined as

---

[1] Published in Sudilovsky et al. (2013)

$$dP = n[1 + w(\theta)]d\Omega, \tag{5.1}$$

where dP is the probability of finding an object within a solid angle $d\Omega$ at an angular distance θ (Peebles 1980). In general, a positive w implies some enhancement of object-object grouping above a uniform random distribution, while a negative w implies some avoidance. The two point correlation function has been used to estimate the clustering properties of galaxies, quasars, and GRBs (see e.g. Groth & Peebles 1977; Ross et al. 2009; Brainerd et al. 1995).

In this work, we measure the angular two-point correlation function between GRB afterglows and field galaxies, and compare this quantity with galaxy-galaxy and AGN-galaxy correlations. We construct two samples, one with only GROND data and one with GROND and Spitzer data.

5.2 Galaxies around GRB sight-lines: I.GROND

5.2.1 The sample

The gamma-ray burst optical and near-infrared detector (GROND) is a simultaneous 7-channel imager mounted on the MPG/ESO 2.2m telescope at La Silla, Chile (Greiner et al. 2008). The four optical channels are nearly identical to the SDSS $g'r'i'z'$ filters, while the infrared channels are effectively equivalent to the 2MASS JHK filters. While the detector system was built to quickly measure photometric redshifts of GRBs via the Lyman-α dropout technique, the multi-wavelength photometry provided by GROND can potentially reveal a wealth of physical characteristics of any source (Greiner et al. 2008).

Our sample of GRB fields is constructed exclusively of GROND observations taken between 2007-2012. This fact ensures a high degree of homogeneity, as no correction for cross-instrumental calibrations are required. Furthermore, the simultaneous nature of GROND observations ensures that data on a per-field basis have not varied due to intrinsic variability or weather conditions. Since only ephemeris, hardware failure and weather losses prevent GROND follow-up observations, the GROND sample of GRB afterglows has an exceptional success rate of $\sim$ 90% detection of long-duration GRBs when follow-up is possible within the first few hours after the trigger (Greiner et al. 2011; Krühler et al. 2011). We include in our sample all fields which 1) have a XRT localization of the burst, 2) Galactic latitude $|b| > 10°$, 3) at least 15° from the Galactic center, and 4) have been observed to a 3 σ background limiting magnitude of $\mathrm{K_{AB}} \sim 20.4$. This limiting magnitude corresponds roughly to an integration time of 1500 and 1200 seconds in optical and near infrared (NIR), respectively, among four telescope dither positions. For reference, typical 3σ AB limiting magnitudes in the optical are at least 3 mag deeper than K, while J and H are 1.0 and 0.5 mag deeper, respectively. Our final sample consists of 73 GRB fields (see Table 5.1 and Fig. 5.1). Since most of the bursts have no measured redshift, we assume that our bursts follows the same redshift distribution as in the TOUGH sample (Jakobsson et al. 2012).

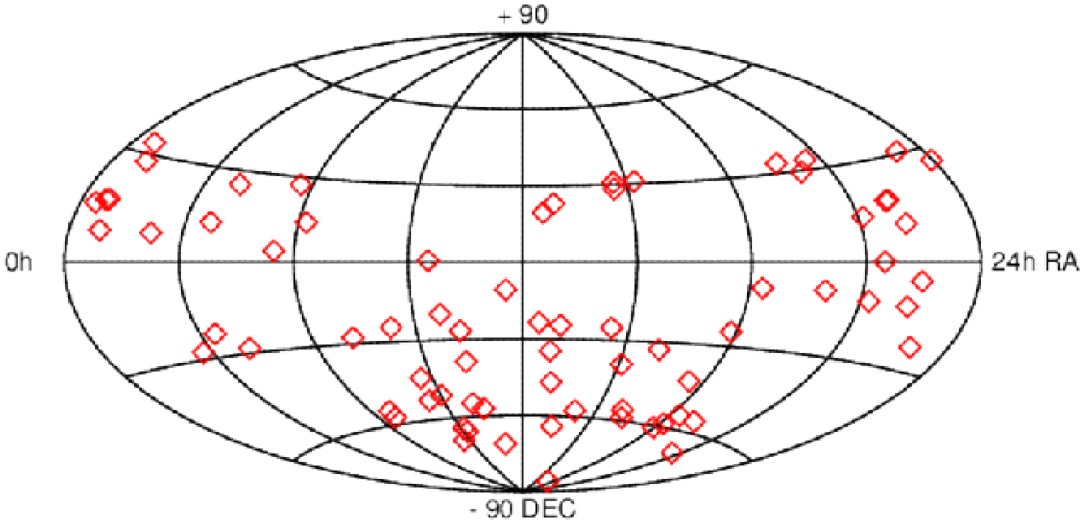

Figure 5.1 Positions in equatorial coordinates of the 73 GROND GRB afterglows in the sample. Bursts within 10° of the Galactic plane are excluded.

Table 5.1: Identification and positions (GROND detection, or XRT if no GROND detection) of the GRB afterglows in the final sample. Typical positional errors for GROND are $< 0.3''$, and $2''$ for XRT. No objects that with localization worse than $2''$ are included.

GRB	R.A. J2000	Dec. J2000
071112C	02:36:50.93	+28:22:16.68
080212	15:24:35.42	-22:44:29.70
080330	11:17:04.51	+30:37:23.48
080408	07:38:39.59	+33:18:14.90
080413B	21:44:34.67	-19:58:52.40
080413	19:09:11.74	-27:40:40.30
080514B	21:31:22.69	+00:42:28.90
080520	18:40:46.30	-54:59:31.00
080523	01:23:11.70	-64:01:51.50
080605	17:28:30.05	+04:00:55.97
080710	00:33:05.67	+19:30:05.69
080916	22:25:06.20	-57:01:22.90
080928	06:20:16.82	-55:11:59.30
081008	18:39:49.89	-57:25:52.80
081109	22:03:09.86	-54:42:41.04
081118	05:30:22.18	-43:18:05.30
081121	05:57:06.08	-60:36:09.94
081228	02:37:50.89	+30:51:09.10

081221	01:03:10.19	-24:32:52.20
081230	02:29:19.53	-25:08:51.72
090102	08:32:38.10	+33:11:45.30
090123	00:27:08.74	-23:30:04.00
090205	14:43:38.65	-27:51:10.70
090323	12:42:50.29	+17:03:11.60
090401B	06:20:21.10	-08:58:19.35
090423	09:55:33.29	+18:08:58.00
090424	12:38:05.09	+16:50:14.75
090426	12:36:18.04	+32:59:09.24
090509	16:05:39.01	-28:23:59.64
090516	09:13:02.59	-11:51:14.90
090519	09:29:07.00	+00:10:49.10
090530	11:57:40.51	+26:35:38.40
090812	23:32:48.54	-10:36:17.60
090814	15:58:26.35	+25:37:52.42
090902B	17:39:45.41	+27:19:27.10
090926B	03:05:13.94	-39:00:22.20
091018	02:08:44.61	-57:32:53.70
091029	04:00:42.60	-55:57:19.84
091109	20:37:01.80	-44:09:29.60
100219A	10:16:48.50	-12:34:00.50
100414A	12:48:26.93	+08:41:34.40
100518A	20:19:09.33	-24:33:16.56
100621A	21:01:13.11	-51:06:22.46
100902A	03:14:30.96	+30:58:45.23
101023A	21:11:51.23	-65:23:15.61
101219B	00:48:55.34	-34:33:59.26
110128A	12:55:35.10	+28:03:54.10
110206A	06:09:20.04	-58:48:24.91
110312A	10:29:55.47	-05:15:45.20
110407A	12:24:07.49	+15:42:42.16
110709B	10:58:37.11	-23:27:16.76
110721A	22:14:38.19	-38:35:35.70
110818A	21:09:20.89	-63:58:51.80
111008A	04:01:48.22	-32:42:34.09
111107A	08:37:54.65	-66:31:12.40
111129A	20:29:44.14	-52:42:46.48
111209A	00:57:22.70	-46:48:05.00
111211A	10:12:21.70	+11:12:30.00
111212A	20:41:43.52	-68:36:45.00
111228A	10:00:16.01	+18:17:51.80
111229A	05:05:08.84	-84:42:38.70

120119A	08:00:06.94	-09:04:53.83
120211A	05:51:00.89	-24:46:30.79
120302A	08:09:35.54	+29:37:41.05
120311A	18:12:22.16	+14:17:46.30
120320A	14:10:04.30	+08:41:47.26
120404A	15:40:02.29	+12:53:06.29
120422A	09:07:38.42	+14:01:07.36
121024A	04:41:53.30	-12:17:26.48
121027A	04:14:23.45	-58:49:47.17
121217A	10:14:50.51	-62:21:03.28
121229A	12:40:24.29	-50:35:39.48

5.2.2 Procedure

Creating the source catalog

To accurately measure the optimal extraction region and measure the apparent extent of sources from GROND multi-band images, we co-add all 7 images to create a single detection image for every field. Since the exposure time differs between the NIR and optical channels, we scale and weigh the images to a common effective exposure. SExtractor (Bertin & Arnouts 1996) is run on the detection image using relatively low source extraction thresholds such that 5-10% of the sources are likely spurious detections, but still no bright sources are incorrectly de-blended or otherwise split into multiple sources. The detection image source catalog is correlated with each individual band's source catalog, and only those sources whose 1) positions in each catalog are consistent to within $0\farcs5$ of each other, and 2) are detected in at least 6 out of the 7 bands (one of which is required to be a K-band detection), and 3) have an error $\sigma_K \leq 0.10$ mag are used in the final source catalog for that field. The latter criteria limits the overall sample to roughly $\sigma_K < 19.3$, with $\sim 10\%$ of sources dimmer than this. The incompleteness down to $K \sim 20.0$ does not introduce any significant bias in the final results. This cross-correlation ensures that spurious detections are removed, and that each source has multi-wavelength detections. The requirement that objects be strongly detected in K ensures that they can be reliably separated between galaxies and stars.

Creating a source catalog based on a detection image in the aforementioned manner minimizes the probability that flux from extended objects is missed due to varying spectral properties as a function of position. That is, by determining a suitable aperture from the co-added image, one is guaranteed that the entirety of flux in an extended source is included therein if that same aperture is then used in each individual image, as long as that source is strongly detected in each band. Additionally, if the source is reasonably isolated in the image, this method avoids the complications introduced by PSF matching and galaxy fitting while still providing adequate photometry. We therefore perform aperture photometry with SExtractor in dual-mode, which uses the detection image as the template against which to perform photometry for each band.

The SExtractor magnitudes are calibrated based on time-tabulated instrumental zeropoints in the case of the optical channels and 2MASS field stars in the case of the NIR. GROND zeropoints are calibrated on average once every three months based on SDSS standard fields, and immediately after technical work is performed on the optical system. The RMS of the optical zeropoints as a function of time is on the order of 0.05 mag. We expect a similar spread due to varying atmospheric conditions, as the range of seeing in our sample is between 1.0 and 1.6 in r'. In 18 fields (24%) co-incident with the SDSS, magnitudes were calibrated directly against SDSS field stars.

Next, we fit each object's spectral energy distribution (SED) with *LePHARE* (Arnouts et al. 1999; Ilbert et al. 2006). *LePHARE* is a spectral template fitting tool based on χ^2 minimization. We determine the best fit galaxy and stellar templates for each source, using the COSMOS galaxy templates, with emission lines and prescribed reddening and parameters therein (Ilbert et al. 2009). More specifically, we adopted the Prevot (Prevot et al. 1984) extinction law for late type galaxy templates and the Calzetti law (Calzetti et al. 1994) and two modifications thereof (Ilbert et al. 2009) for the SB templates. The values of extinction range from $0.0 < E(B-V) < 0.5$ in steps of 0.1. Early type galaxy templates are not corrected for extinction, as there are no well-tested empirical models to describe the dust distribution for these galaxies. In the case of galaxy templates, redshift is constrained to $z < 2$ with a step size $\Delta z = 0.01$. The former constraint removes some degeneracy between high and low redshift template fits, and is justified since the population of galaxies with an apparent $\mathrm{K_{AB}} < 20.0$ is negligibly small at $z \gtrsim 1.5$. We assume that the contamination from AGN-dominated sources in our galaxy catalog is negligible ($\lesssim$ 5%, as discussed later). We separate galaxies and stars based on their best fit template and shape parameters. Any sources with a full-width half maximum (FWHM) or ellipticity as measured with SExtractor in 5σ excess of the stellar values for that field are automatically classified as galaxies. These stellar values are determined by computing the average and standard deviation of the lowest 20% FWHM and ellipticity distributions, under the assumption that those "bottom 20%" of sources are stars. In practice, this usually means the FWHM and ellipticity of 5-10 stars are averaged for a given field. Besides this shape criterion, we categorize sources with $1.5 \times \chi^2_{\mathrm{star}} > \chi^2_{\mathrm{galaxy}}$ as galaxies, where χ^2 corresponds to the best fit template for that class of source. This latter criterion has been applied to the COSMOS field with great success (Salvato et al. 2009). The extinction law and extinction values are to some extent free parameters in the fitting. Therefore, a certain amount of degeneracy in redshift-color-extinction space is expected. However, we do not expect this degeneracy to affect star/galaxy classification. This is due to the consideration of morphological information (i.e. extended vs point-like) and the implied redshift limit imposed by the K band magnitude limit. The process of classifying stars from galaxies is not straightforward in most cases, as shown in Fig. 5.2.

We detect 3068 galaxies and 1368 stars that match our criteria. The K-band magnitude distribution of galaxies is presented in Fig. 5.3.

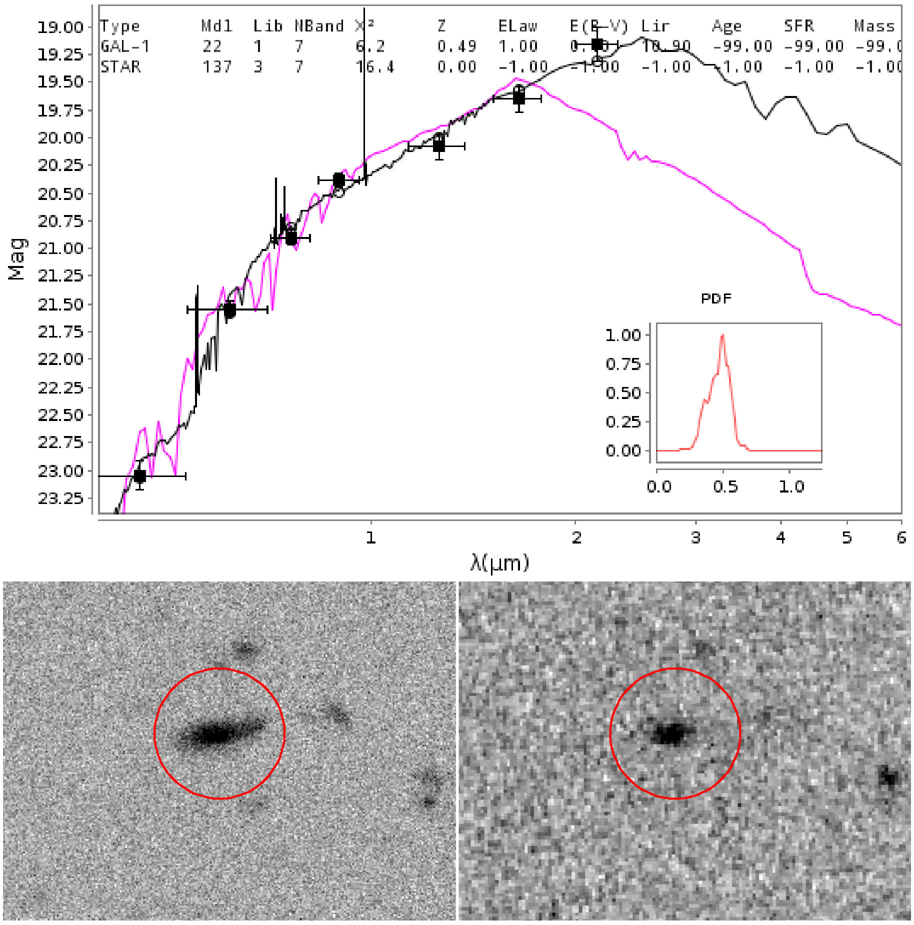

Figure 5.2 (Top) The lePHARE spectral energy distribution for a galaxy in the COSMOS-30 catalog. The black and pink lines are the best fit galaxy and stellar template, respectively. The inset shows the probability distribution function of the resulting redshifts derived from the galaxy fit. The K-band magnitude is crucial to distinguish stellar and galactic templates, and even with very strong detections, the redshift determination is not well constrained with only these data. (Bottom) The g' and K_s image counterparts to the lePHARE fit. The source is clearly extended in g', but is not distinguishable from point-like in K_s. A dimmer or more elliptical galaxy would not be classifiable by shape parameters. These images show an ideal case of star/galaxy characterization, and illustrate the inherent difficulty in such a process.

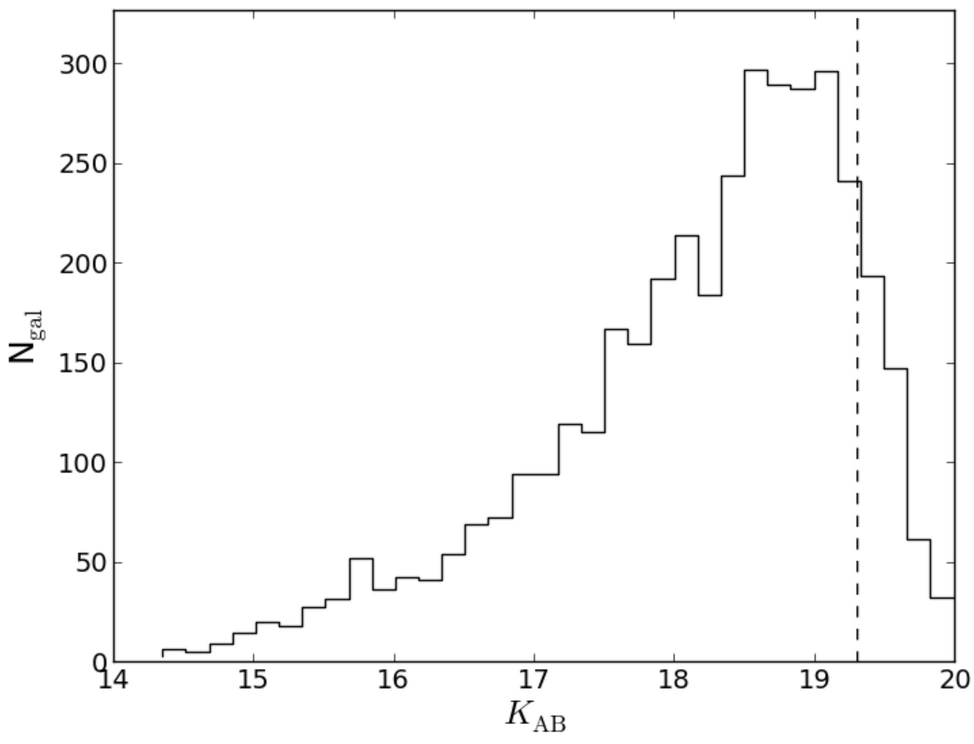

Figure 5.3 K_{AB} magnitude distribution of the 3068 field galaxies identified in the sample. The steep drop-off after $K \sim 19.3$ is due to the criteria that $\sigma_K \leq 0.10$ for each galaxy, and that is it detected in five other bands. This represents a decline in completeness of the sample. The typical 3σ limiting magnitude for an individual image as determined from the sky background is $K_{AB} \sim 20.4$.

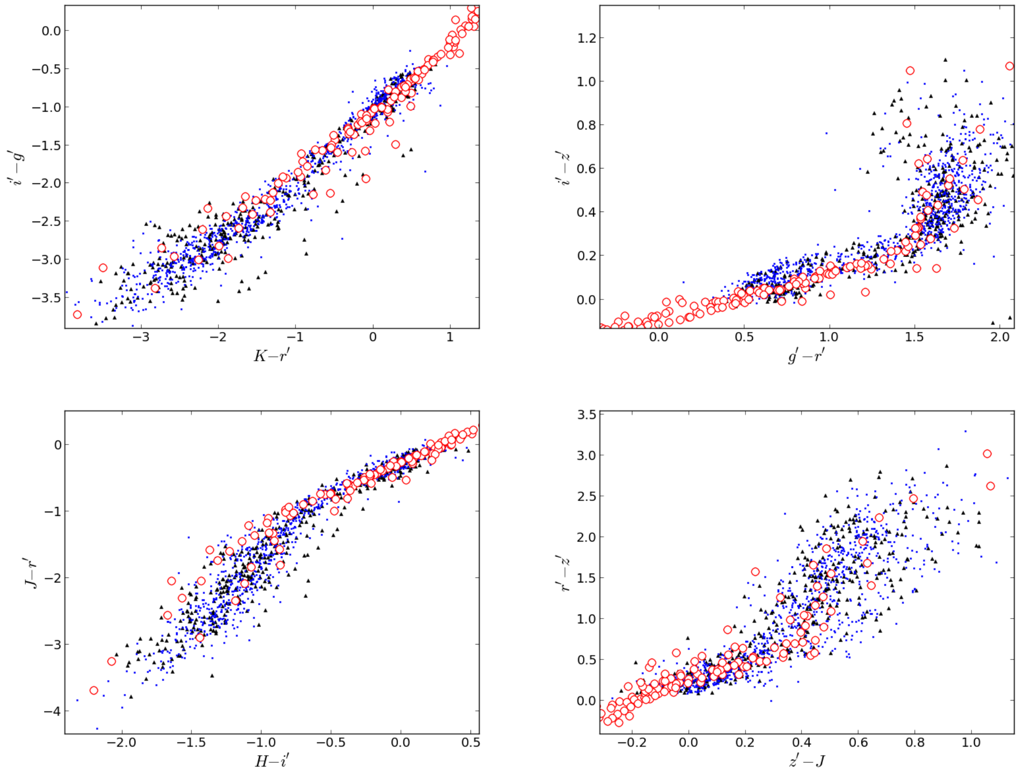

Figure 5.4 Color-color diagrams for stellar templates (open circles) and sources identified as stars (black triangles and blue squares) in the GROND sample. Offsets of +0.2, +0.08, +0.08, and +0.1 mag to the g', r', i', and z' zeropoints are applied, except in the case of direct SDSS calibration. The sources represented by black triangles are SDSS calibrated, while the blue squares represent a zeropoint calibration.

Verifying the source catalog

To determine the accuracy of our galaxy-star separation, we compare a catalog of sources derived from nine GROND sub-fields of the COSMOS field with the COSMOS 30-band photometric catalog (COSMOS-30; Ilbert et al. 2009). COSMOS-30 has much larger spectral coverage and higher sensitivity than the GROND observations, making it an ideal standard with which to compare. We employ COSMOS-30 as both a measure of the quality of galaxy identification from GROND and to calculate the AGN-galaxy two point correlation function. From the nine adjacent sub-fields observed by GROND (center pointing at R.A.=150.0862 deg, Dec.=2.3745 deg), we identify 317 total candidate galaxies. Nine of these candidates are in a masked area in COSMOS-30, and a further nine are categorized as stars in COSMOS-30. This corresponds to 2.9% of galaxies that are misclassified using our method, assuming COSMOS-30 has 100% accuracy in classification. Besides the masked objects, no candidates were detected in GROND images without a corresponding source in COSMOS-30. The lack of spurious detections is likely a result from our stringent detection criteria discussed in §5.2.2 – namely, that an object must have independent detections in at least six filters.

We evaluate our photometric calibration by comparing the colors of sources that we classify as stars to the stellar templates of Pickles (1998) and Bohlin et al. (1995). In Fig. 5.4, we present color-color diagrams of our sources compared with those of stellar templates. On average, offsets of +0.2, +0.08, +0.08, and +0.1 mag to the g', r', i', and z' zeropoints, respectively, are required to match the colors of the stellar templates. In the case of direct SDSS calibration, no offset is needed nor applied. After applying these offsets, the colors of stars in our catalog are on average not offset from those of stellar templates, implying a reliable photometric calibration. The somewhat higher scatter of our objects relative to the templates is due to a combination of uncertain dust extinction towards foreground stars, binary systems, and photometric uncertainty.

Measuring the two-point correlation

After the source catalog is categorized, calculating a two-point GRB-galaxy correlation function is possible. Since our sample consists of isolated fields with no overlap, we must calculate distance pair distributions on a field by field basis, later combining them into a global correlation function. This technique limits the angular sizes we can examine, and furthermore introduces systematic errors when the size scales approaches the size of individual images. However, since we are specifically examining clustering at small scales, GROND's $5.4' \times 5.4'$ images[2] have sufficient spatial coverage. We limit our our analysis to angular distances $\leq 120''$. This angular distance corresponds to $\sim$ 600 kpc at $z = 0.4$, assuming a ΛCDM concordance cosmology with $h = 0.7$ and $\Omega_m = 0.27$ (Wright 2006).

Many of the afterglows in our sample have no measured redshift. We assume that our sample of GRB afterglows has an underlying redshift distribution that is consistent with the literature (Jakobsson et al. 2012). More specifically, the GRBs should be *background* to the galaxies in the field. This latter assumption is likely justified, since the mean redshift of GRBs is $z \sim 2$ and the mean redshift of galaxies with $K < 19.3$ is $z \sim 0.4$, as noted in §5.2.1.

To measure the two-point correlation, we start by calculating the angular distance between the GRB optical afterglow positions (or the XRT afterglow position circle, in the case that no optical afterglow was detected) and each galaxy. This provides a distribution of arclengths n_{DD} for a given field. Next, we assign a new position to each galaxy within that field based on values picked from a uniform random distribution. Any galaxies that are within two stellar FWHM of a star or fall into an object mask are re-assigned a position until they do not. This ensures that the observability of the isotropically distributed control sample shares the same observational properties as the actual galaxies. We calculate the distances between each GRB-random galaxy n_{DR} and the random sample's mutual separation n_{RR}. This process is repeated and averaged over

---

[2] $5.4' \times 5.4'$ in $g'r'i'z'$, $10.3' \times 10.3'$ in JHK

a total of 10^3 times for each field. We then calculate the angular correlation function w and its variance σ using the Landy & Szalay (Landy & Szalay 1993) estimator

$$w = \frac{DD - 2DR + RR}{RR}, \tag{5.2}$$

$$\sigma_w^2 = \frac{1 + w}{n_{DD}}, \tag{5.3}$$

where DD, DR, and RR are the normalized frequency distributions of n_{DD}, n_{DR}, and n_{RR}, respectively. We perform the same procedure to measure $w_{galaxy-galaxy}$, $w_{AGN-galaxy}$, and $w_{random-random}$. Though it is trivial to show analytically that w is zero in the case of isotropically distributed data, we explicitly perform the calculation using three randomly chosen coordinates per field as a verification of our method.

We compute the correlation functions on both the GROND and COSMOS-30 sample. To approximate the same selection criteria and completeness of our GROND sample, we remove from the COSMOS-30 catalog any sources with $\mathrm{K_{AB}} > 19.3$ as well as those sources whose photometry may be unreliable due to saturation or being within an object mask (No flags in any optical filter). This leaves 4481 galaxies and 2273 stars. The photometric redshift distribution of these COSMOS-30 galaxies is presented in Fig. 5.5. The mean and median redshift of this sub-sample is 0.387 and 0.361, respectively. We ensure that only *background* X-ray selected sources are included in the $w_{AGN-galaxy}$ calculation by imposing a $z > 1.0$ redshift criterion (Salvato et al. 2011). This criterion limits the COSMOS-30 catalog to 980 sources.

5.2.3 Results

In Fig.5.6, we present the two point GRB-galaxy, galaxy-galaxy, and random-random angular correlation functions computed from the GRB sample. The two point correlation functions are self-consistent for all angular distance scales, with the exception of the (as expected) null random-random function. A possible contribution to the first bin of the GRB-galaxy $w_{GRB-GAL}$ is likely due to the detection of the host galaxy of the GRB, although the vast majority of known GRB hosts are fainter than our magnitude limit. This corresponds to $3''$ in our sample, and it is entirely possibly to find GRB host galaxies at up to these distances from the afterglow position and larger. Furthermore, these are also the angular distance scales within which Chen et al. (2009) find sources nearby sight-lines to GRBs with spectroscopically identified intervening MgII systems, albeit at very faint magnitudes.

We also find clustering of galaxies within small angular distances of each other as seen in the galaxy-galaxy correlation $w_{GAL-GAL}$. This is consistent with expectations from multiple galaxies occupying the same massive halo (Berlind & Weinberg 2002; Lee et al. 2006) and naturally from galaxy clusters. This signal is seen more clearly in the correlation function as measured from the COSMOS-30 sample (Fig. 5.7), where we include only sources with $\mathrm{K_{AB}} \leq 19.3$ to approximate our sample's completeness. For the COSMOS-30 sample, the best fit power-law to the first 14 bins ($0 \leq \theta \leq 42''$)

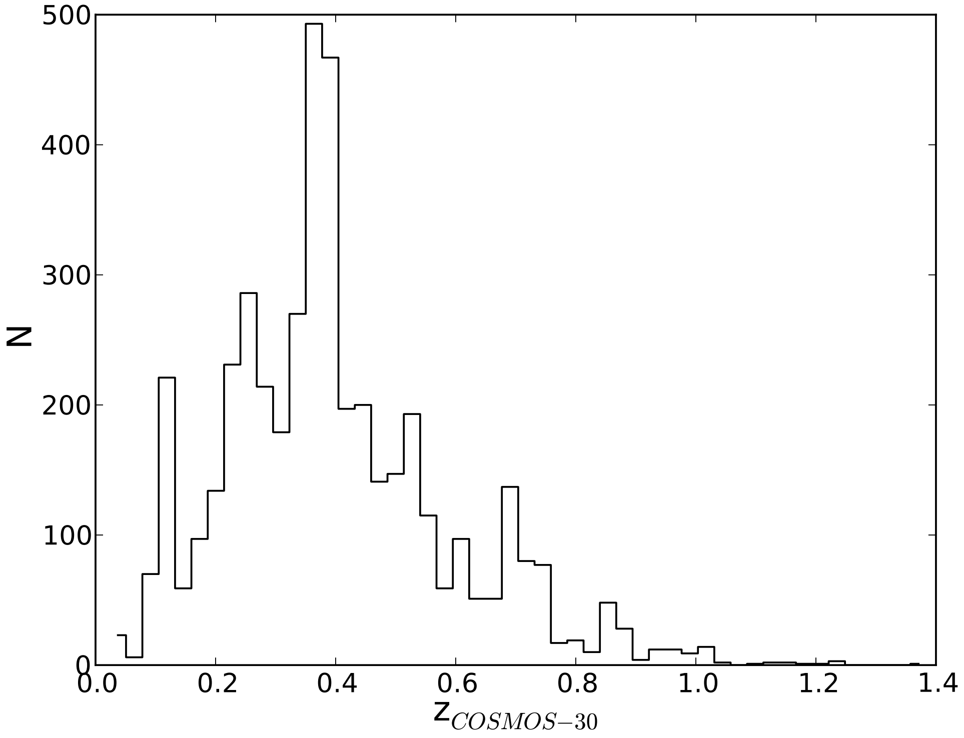

Figure 5.5 Photometric redshift distribution of the 4481 galaxies in COSMOS-30 that have $K_{\mathrm{AB}} < 19.3$. The mean and median redshifts of the distribution are 0.387 and 0.361, respectively.

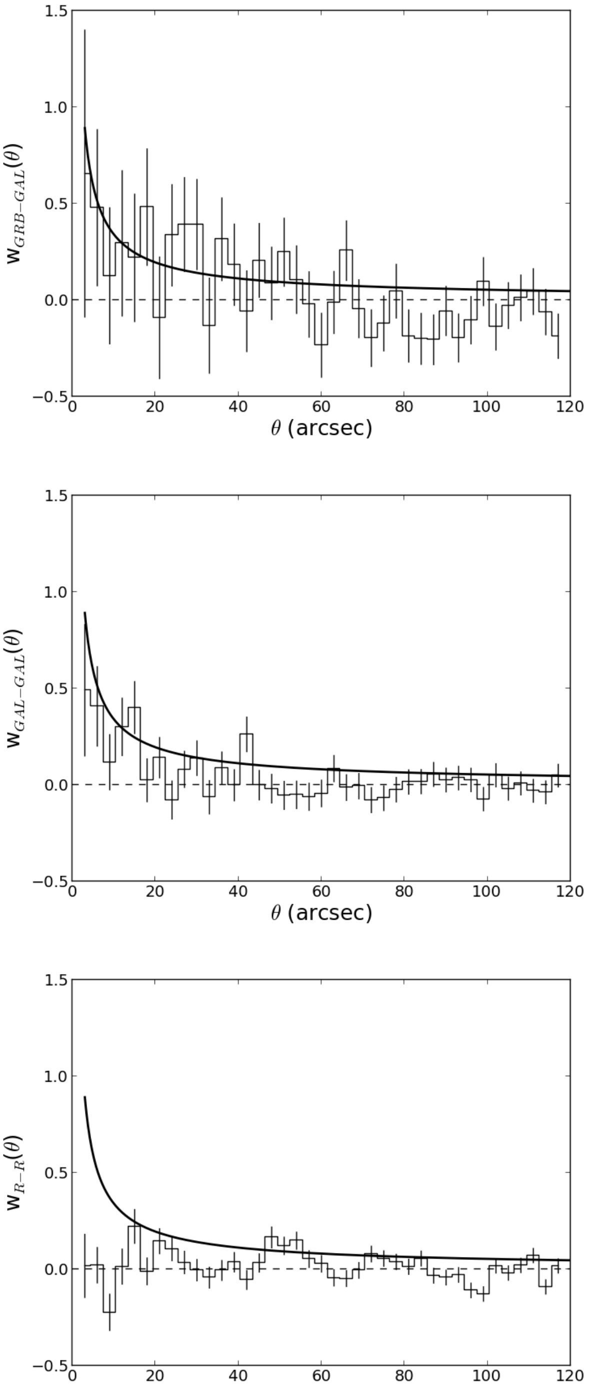

Figure 5.6 (Top to bottom) GRB-galaxy, galaxy-galaxy, and random-random two point correlation functions. The solid black line represents the best fit power-law to the COSMOS-30 galaxy-galaxy two-point correlation function, as described in Fig. 5.7 and in §5.2.3. The random-random two-point correlation function is, as expected, consistent with zero.

of the form $(\theta/\theta_0)^{-\delta}$ yields a correlation length $\theta_0 = 2.6 \pm 0.4$ arcseconds and slope $\delta = 0.8 \pm 0.2$ (statistical error only). This same power-law is presented in all two-point correlation functions for comparison.

The AGN-galaxy two-point correlation function $w_{AGN-GAL}$ is also presented in Fig. 5.6.

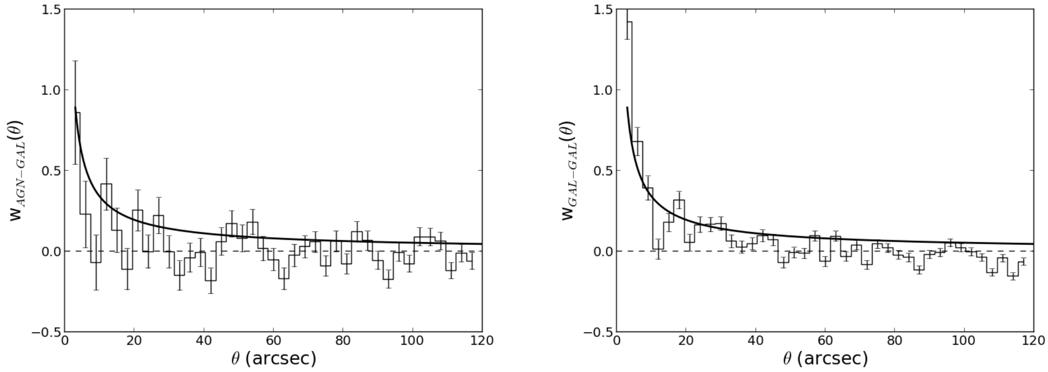

Figure 5.7 (Left to right) AGN-galaxy and galaxy-galaxy two-point correlation functions computed from the COSMOS photometric catalog. To approximate the GROND sample selection and completeness, only sources with $K_{\mathrm{AB}} < 19.3$ are included. The best fit power-law of the first 14 bins ($0 \leq \theta \leq 42''$) of the galaxy-galaxy two-point correlation function is represented by the solid black line. The same fit is used in both figures for comparison.

5.3 Galaxies around GRB sight-lines: II. Spitzer & GROND

5.3.1 The data

To increase the depth and wavelength of the survey, we include data from the Spitzer warm mission (IRAC channels 1 & 2) for pointings with coincident GROND coverage. Typical data of GRB host fields taken with Spitzer have limiting magnitudes of at least $\sim 26\mathrm{mag_{AB}}$. This effectively limits the survey to GROND optical, which is typically 3 mag deeper than GROND NIR.

Unfortunately, only 28/73 = 38% of the sample described in section 5.2 have Spitzer coverage. Still worse, the high sensitivity of IRAC causes increased saturation and blending of bright sources, leading to more and larger masked areas, as shown in Figure 5.8. Naturally, this leads to less usable area in the sample and thus negatively impacts the number of sources detected. However, since we are most interested in the area immediately near the GRB position, this is not expected to affect our results.

We obtained Spitzer data and their corresponding uncertainty images from the Spitzer Heritage Archive (SHA). The level 2 (PBCD) data products provided by the SHA are reduced, astrometerized, and flux-calibrated.

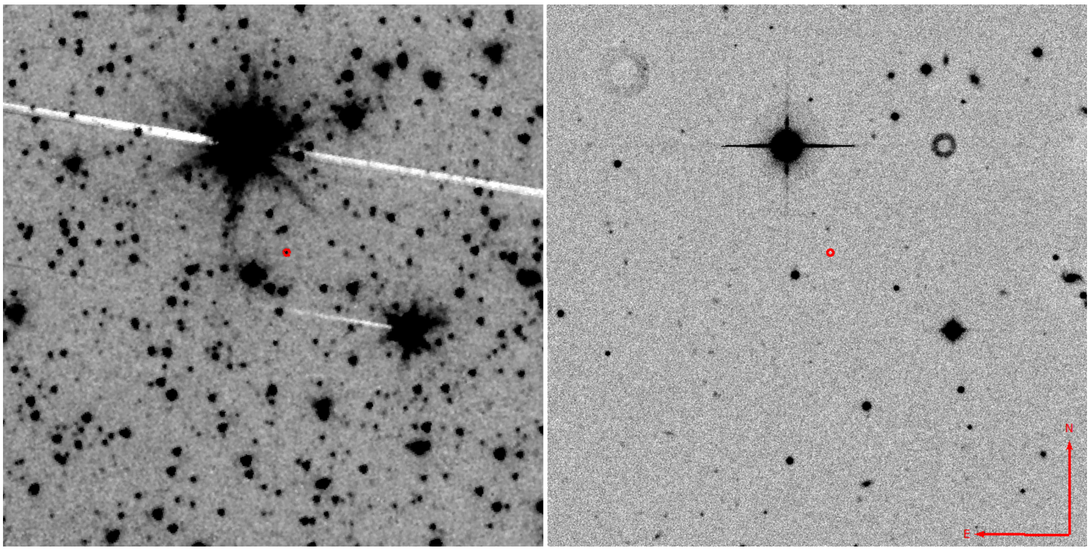

Figure 5.8 Spitzer IRAC Ch. 1 (left) and GROND r' (right) image of the field of GRB 090407. The 1.4″ enhanced XRT afterglow position is illustrated by the red circle. The significantly higher sensitivity of the IRAC data allows the detection of many otherwise undetectable sources in GROND, although saturation and blending of sources occurs more frequently.

5.3.2 Methods

In general, we follow the same source extraction and classification strategy as outlined in §5.2.2. However, since the point-spread function of Spitzer is significantly larger than the typical atmospheric seeing in the GROND sample, extra care must be taken not to mismatch a source between GROND and Spitzer, especially if sources are blended. To this end, we adopt the same method as applied to the COSMOS survey. We perform aperture photometry using a 1.4″ aperture independently, and cross-correlate the GROND and Spitzer extracted sources based on position. Though this process is expected to lead to a larger fraction of mismatched sources than using the same aperture throughout all filters, we find that significantly increased photometric accuracy justifies this decision.

To quantfy the photometric accuracy of the newly incorporated Spitzer data, we apply our source extraction and analysis pipeline to a subsection of the COSMOS-30 field. In Fig. 5.9, we compare the AB magnitudes of sources extracted using our method with the COSMOS-30 catalog. We conclude that our photometric pipeline produces results that are fully consistent with the COSMOS catalog.

An additional important distinction from §5.2.2 is in the number of bands in which we require the detection of a source. Instead of detections in 6 out of 7 band, we require at least 3 detections in any of the GROND filters, and additionally a corresponding independently detected counterpart in IRAC Ch.1. We apply this criteria since the energy

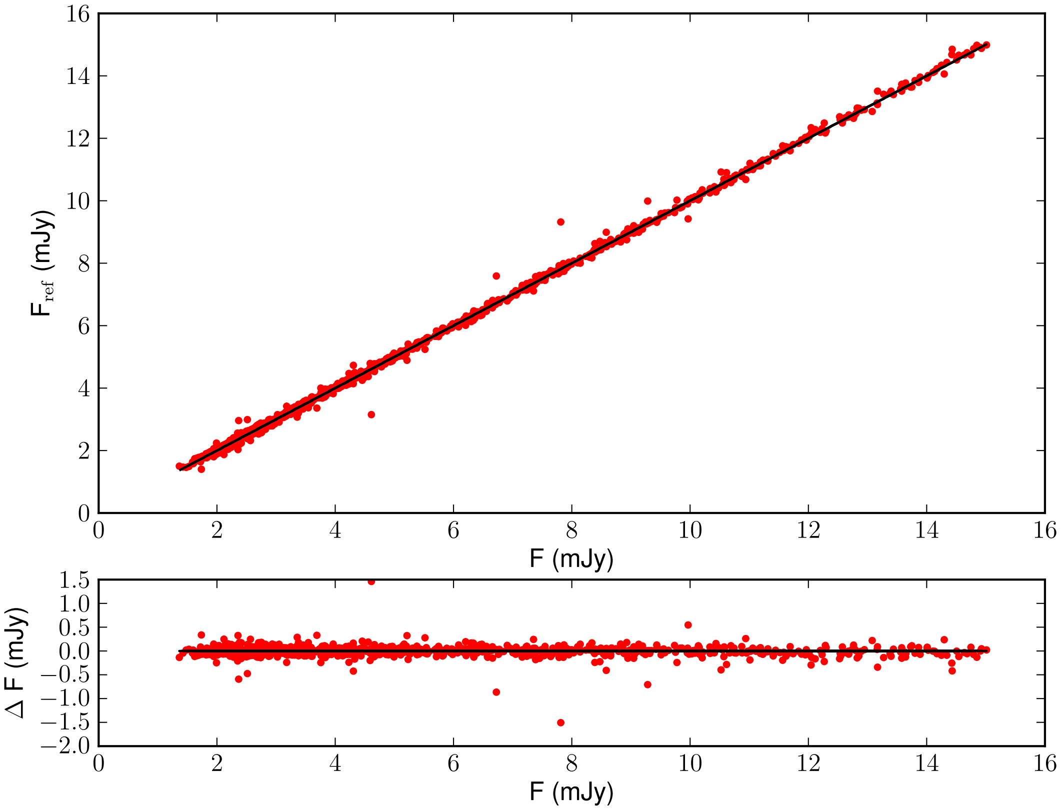

Figure 5.9 COSMOS-30 vs our independently estimated IRAC Ch. 1 magnitudes of 1359 sources in the COSMOS field and residuals. The standard deviation of the residuals is $\sigma_F = 0.11 mag$. Both samples are mutually consistent.

regime probed by Spitzer as extremely helpful in distinguishing stars from galaxies.

Using this method, we detect and categorize a total of 4135 galaxies and 389 stars in the combined GROND/Spitzer images. As a reminder, we detected 3068 galaxies and 1368 in the sample described in §5.2.2. The ratio of galaxies to stars in a survey is a good indicator of its depth. The log N-log S distribution of stars flatten towards lower flux, while the population of galaxies continues to increase. For this reason, we detect more galaxies in the GROND/Spitzer sample than in the GROND sample, even though the former has a significantly smaller survey area.

As in §5.2, we find that photometric redshifts are reliable only as a statistical measure – there is no guarantee that an individual object's photometric redshift is well constrained. For this reason, we do not perform a two point distance correlation analysis, instead limiting our results to the integrated global properties of the galaxies in the field. Even more importantly, binning the sample by redshift or attempting to calculate the two-point proper distance correlation function would reduce the statistical significance of the results to null.

5.3.3 Results

In Fig.5.10, we present the two point GRB-galaxy, galaxy-galaxy, and random-random angular correlation functions computed from the GROND/Spitzer sample. As in §5.2, the GRB-galaxy and galaxy-galaxy correlation functions are mutually consistent.

This result supports the conclusion that there is no excess of galaxies near GRB afterglows down to $r' \sim 23$, integrated over all redshifts visible to that magnitude limit. Naturally, the signal of galaxies clustered around the GRB event at close cosmological distances may not be detectable if those galaxies do not compromise a significant fraction of the total galaxies observed. If this is this case, then such a signal would be smeared out unless the survey a) had enough sources to maintain statistical significance even when the sample were finely binned in redshift space, and b) could accurately determine the redshift of each source to smaller than the redshift bin or typical separation distance.

5.4 Discussion

A $w_{GRB-gal}$ that is consistent with $w_{GAL-GAL}$ and $w_{AGN-GAL}$ implies that there is no excess or unusual clustering of galaxies around GRB events, contrary to the expectation from observations of MgII absorption line systems. Though our data support this null hypothesis, one must consider that the limiting magnitude of our sample is relatively shallow in comparison to the expected magnitudes of galaxies hosting MgII absorbers at the redshifts found in GRB afterglow spectra. Indeed, the typical magnitudes of candidate absorption line counterparts detected by Schulze et al. (2012) have $K_{\rm AB} > 22$, and Chen et al. (2009) find that the objects at angular distances of sources $1'' - 3''$ to GRB hosts with spectroscopically detected MgII typically have $H_{\rm AB} \gtrsim 26$.

Although we expect that an overdensity of MgII absorbers corresponds to an overdensity of galaxies around the line of sight, we are unfortunately limited to the very brightest and closest objects in our survey. A qualitative measure of how much low number statistics affect w is demonstrated by comparing our galaxy-galaxy correlation with that calculated from COSMOS-30 (Figs. 5.6-5.7). The correlation as measured by 3068 galaxies in GROND fields only shows a hint of clustering due to halo occupation of multiple galaxies and galaxy clusters, as discussed in § 5.2.3. The signal is much more clear from the 4481 galaxies with $K_{\rm AB} < 19.3$ that we extract from COSMOS-30.

Clustering analysis of GRB afterglows and/or hosts have been performed by Wang & Wei (2010); Bornancini et al. (2004). Wang & Wei (2010) find no evidence of clustering between *SWIFT* XRT afterglows and *ROSAT* selected galaxy clusters. The purpose of our survey is not to examine large scale anisotropies, but rather the small scale clustering implied by the MgII excess. Bornancini et al. (2004) examined whether GRB host galaxies tend to reside in high density environments by calculating the GRB-galaxy two point correlation for 19 GRB hosts. They concluded that GRB host galaxies likely do not occur in over-dense areas, although local cosmic variance could still significantly affect these results due to the small sample size. Furthermore, choosing hosts over

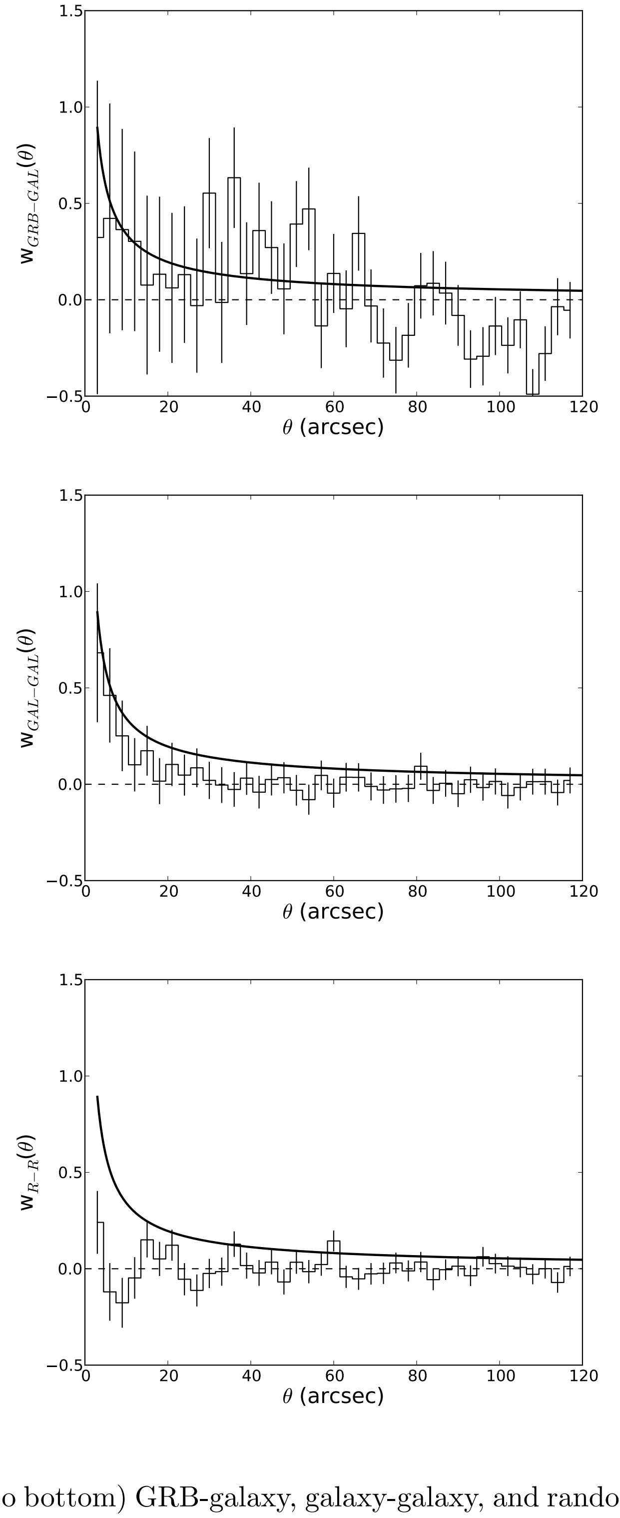

Figure 5.10 (Top to bottom) GRB-galaxy, galaxy-galaxy, and random-random two point correlation functions. The solid black line represents the best fit power-law to the COSMOS-30 galaxy-galaxy two-point correlation function, as described in Fig. 5.7 and in §5.2.3. The random-random two-point correlation function is, as expected, consistent with zero.

afterglows introduces an additional bias against intrinsically dim or reddened hosts. Constructing a sample based on afterglow positions – as done in this work – removes this bias and increases the sample size significantly. Furthermore, there is no a priori reason to link foreground absorption in the afterglow with the detection or non-detection of a host galaxy.

The results from the clustering analyses supports the conclusion that there is no excess of galaxies near GRB afterglows down to $r \sim 23$, integrated over all redshifts visible to that magnitude limit. Naturally, the signal of galaxies clustered around the GRB event at close cosmological distances may not be detectable if those galaxies do not compromise a significant fraction of the total galaxies observed. If this is the case, then such a signal would be smeared out unless the survey a) had enough sources to maintain statistical significance even when the sample were finely binned in redshift space, and b) could accurately determine the redshift of each source to smaller than the redshift bin or typical separation distance.

Even though this is a fundamental limitation of the survey, one must keep in mind that the MgII discrepancy is very likely to originate from intervening systems. This being the case, we expect that any over-density of field galaxies implied by the MgII issue would be distributed evenly towards the GRB, and thus discerning correlations as a function of redshift is not vital.

It is important to keep in keep in mind that the distribution of galaxies with and apparent $r > 23$ falls steeply after $z > 1$. Therefore, our survey only probes potential counterparts of MgII absorbers up to that redshift. The redshift distribution of MgII absorbers (as determined from spectroscopy) is seemingly uniform within its detection range of $0.4 < z < 2.0$. If we assume that this uniform distribution is also valid for our survey of $0 < z \lesssim 1$, one can estimate the expected number of absorbers per GRB in our sample. If one takes $dn/dz = 0.24$ as per quasar statistics, then we expect 17.52 (6.72) counterparts in the GROND (GROND+Spitzer) samples. A $dn/dz = 0.60$ as per GRB statistics yields 43.8 (16.8) expected absorbers, or a $\sim 250\%$ increase, which should be reliably detected in our survey. Of course, these values assume 100% completeness, and therefore for a more realistic estimate must be weighted by the luminosity function of MgII counterparts. Unfortunately, there are currently not enough confirmed MgII counterparts detected to construct such a luminosity function.

Chapter 6

GrondView

6.1 Improvements on remote observing

Over the past years, the remote operation of GROND has become a priority. GROND was built to accept and execute RRM without human intervention. To extend the capability of remote observation, we have implemented several improvements:

- Automatic upload of every new readout to a website viewable by the GROND team, allowing a near real time view of the telescope FoV.
- Command-line tool to create and upload user defined image cutouts with analysis results, allowing the near real time inspection of reduced data products without the high bandwidth requirements of X11 forwarding.
- Synchronization of raw GROND data products from the ESO data archive with local MPE servers once/day
- Synchronization of raw GROND data products with a dedicated data reduction computer at La Silla Observatory once every 5 minutes.

These improvements have allowed our team to perform roughly 50% of our observational time remotely, mainly by significantly lowering the analysis time of new GRB triggers.

Future improvements include increasing the flexibility of our existing automatic data reduction pipeline and automatically initiating telescope guiding as necessary.

6.2 Automatic processing with `bulk_reduce.py`

At the time of this writing, GROND has produced 24 TB of data since 2007. The data are stored on an Andrew File System (AFS), hosted by the Rechenzentrum Garching (RZG). The data are sorted in a hierarchical fashion on the file-system with the schema `YYYY-MM-DD/raw/[targetID]/[OB]/`. Historically, data have been fetched, reduced, and analyzed by individual group members interested in that particular observation. After analysis, the final data products would usually be deleted or otherwise left undocumented. This process includes the following steps:

- Determine the targetID and OB of the relevant observations: Though in most cases these are unique identifiers, in some non-negligible number of cases there exist the same OB name on different nights, and even that the same field was observed with two different targetIDs. Therefore, to obtain a complete dataset, one must look through the manually created observation logs for (hopefully) notes of these cases.
- Copy the data from the AFS to a local disk: An AFS, though highly available, does not offer high I/O speeds. Even under the ideal case of copying the data to a machine on the MPE network, which is directly connected via fiber-optic to the RZG, a *single* observation could take anywhere from a few minutes to a day.
- Run the reduction scripts: Depending on the size of the dataset and the number of objects in the images, reduction could take anywhere from tens of seconds (in the most trivial case) to a few hours (for large datasets of crowded fields).
- Analyze the reduced images: The analysis scripts take usually on order of a few minutes for large datasets, and constructing SEDs or lightcurves of a particular object can take a few tens of minutes to hours, depending on the level of expertise of the individual doing the analysis.

Though this system of operation is perhaps optimal for producing the highest quality, hand-tuned results, it is extremely inefficient in terms of productivity. This method requires the end user to perform a significant amount of bookkeeping in terms of tracking observations and directory paths, it is very time costly, and it has no safeguard against the duplication of work done by others.

In an effort to improve the interaction of scientists with GROND observations, we have developed a framework to optimize the reduction, searching, and storage of data. The end result of this framework, dubbed *GrondView*, is a modern web interface with which a user can interact with GROND data. The framework consists of several steps distributed over two MPE servers with hostnames `sauron` and `faramir`. Both of these machines are automatically and fully backed up daily.

Data produced by GROND are physically transported from La Silla Observatory, Chile to Garching, Germany on USB media on average once every two months. The data are copied to the AFS. Invocation of the script `bulk_reduce.py` will perform the following operations:

- Recursively search the target directory for any GROND data
- Update a sqlite3 database on `sauron` if the data are new, and assign a correct OB identifier based on previous observations under that targetID

- Run the GROND data reduction pipeline (reduction and analysis) on each observation found, storing all logging output in the aforementioned sqlite3 database.
- Store the success/failure status of the reduction in the database, including at which point the processing failed.
- If the pipeline has reduced the observation successfully, move the resulting reduced data products to a staging area.

In practice, `bulk_reduce.py` is manually invoked on all new data arriving via USB media from La Silla Observatory. The time to completion for 2 months of data varies from 2-4 weeks, depending on how frequently GROND observed. `bulk_reduce.py` is designed to run to completion regardless of any type of failure of processing, to skip already successfully processed observations, and to re-attempt those that failed. These options may be changed with command line flags at runtime.

At present, there have been a total of 1808 observations processed automatically, of which 1287 have been flagged as completely and successfully reduced, and 725 have been successfully reduced and analyzed. The success rate for GRB and other 'standard' observations is undoubtedly significantly higher, as GROND has been used for a significant fraction of time to monitor planet transits with a very specialized observing strategy, which our pipeline is not designed to process. Additionally, we have decided to classify an observation as successfully processed if and only if each of its seven bands process successfully. In practice, this is a stringent requirement, as the least sensitive bands (g' and K_s) have a higher failure rate in extremely sparse and crowded fields. Resolving at the filter level as opposed to the observation level would also significantly increase the success rate of automatic processing.

The sqlite3 database is designed to be the authoritative document that details which data have been processed and their status. Any user that wishes to include their own self-analyzed dataset in this framework will interact[1] with this database, updating it as needed. The database consists of a single flat table with the following schema:

```
CREATE TABLE data (id INTEGER PRIMARY KEY AUTOINCREMENT,
                    targetid TEXT,
                    date_obs timestamp,
                    ob_native TEXT,
                    ob_corrected TEXT,
                    status_reduction INTEGER,
                    status_analysis INTEGER,
                    problem_bands TEXT,
                    log_warning TEXT,
                    log_critical TEXT,
                    log_error TEXT,
                    log_full TEXT,
```

---

[1] via automated user-friendly command-line scripts

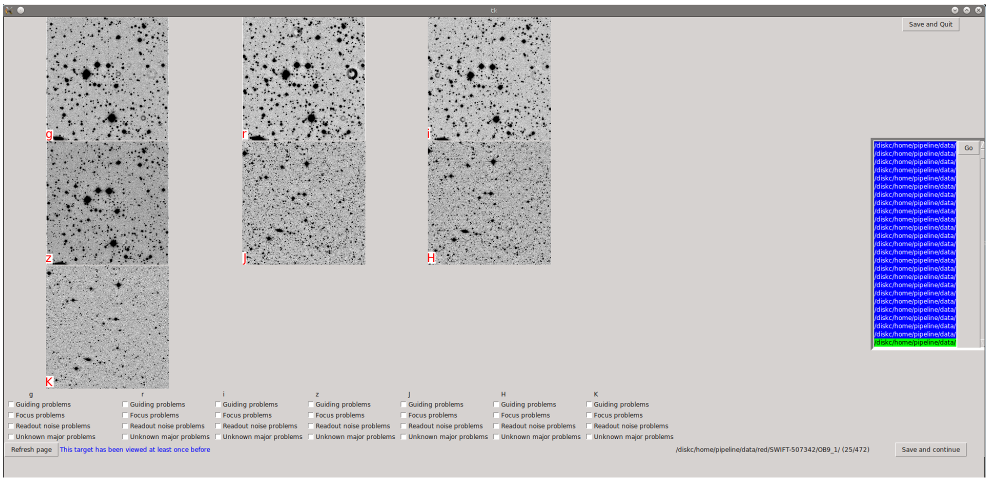

This target has been viewed at least once before

/diskc/home/pipeline/data/red/SWIFT-507342/OB9_1/ (25/472)

Figure 6.1 The GROND processed image viewer, designed for the quick review and flagging of images automatically processed as a final data quality assurance. The python/Tkinter application is designed to load GBs of GROND images asynchronously, allowing the user to rapidly flag images.

```
fits_header TEXT,
date_reduction timestamp,
user_reduction TEXT);
```

6.3 Data Quality Assurance and upload to GrondView

To ensure that only the highest quality data is kept from the automated processing, we have implemented an additional verification of the data. We visually review each image that has successfully passed the automated processing and flag any image that is unsatisfactory. To optimize this process, we have developed a GUI application that asynchronous loads all images (which can be many GB of images) in a directory and takes care of recording the status of individual images. The application in operation is presented in Fig. 6.1. The output of a review session is automatically formatted in a color-coded table and uploaded to a GROND group wiki page.

In practice, on order 1% of observations that have passed the automatic processing checks are flagged as unsatisfactory. Nevertheless, we have decided to continue this practice to ensure the highest quality of data possible.

Observations that have not been flagged by a reviewer are ready to be ingested into the GrondView database. The operator invokes a final script, `pipeline_push.py`, which creates a g-zipped tape archive of the observations and their auxiliary data, uploads the archive to `faramir`, and finally spawns a process therein that unpackages the archives and starts ingestion of the observations. Observations than are reduced and analyzed outside of this framework can be incorporated to the GrondView database as well. Overwrite/update preference is always given to user over automated processing. Ingestion on the `faramir` side is completely independent of user interaction. An email notification is given to the user that initiated the ingestion upon success or failure of the procedure.

6.4 GrondView web interface

GrondView is a web application written in Python/Django with twitter-bootstrap UI, which uses postgreSQL as a database backend and redis as a task broker. The deployment environment is fully defined in a Puppet manifest, allowing for an automated building and implementation of the application on any family of operating system using the `apt` package manager. The application is currently hosted on `faramir`, behind the MPE firewall.

GrondView is designed to facilitate the management of high quality reduced GROND data products. It is a centralized place to search and store image and source specific information. The home page, after login, is presented in Fig. 6.2. Users may search for specific images and sources by position. In the cases of sources, one may further filter based on their number of independent detections, or create add a user generated source associated with their account at a given position. Besides these user generated sources, automatically detected sources are distinguished in the database by having an angular separation of a least $0.3''$, which is a conservative estimate of typical GROND astrometrical precision. Resolving sources to a higher precision requires the user to create a source at its exact position, which is treated independently of automatically detected sources.

A positional search yields a results as shown in Fig 6.3. This output also doubles as a convenient way to quickly obtain cutouts of any area covered by GROND and in the database.

The detailed field and object interfaces are presented in Figs. 6.4 and 6.5, respectively. In the case of the source view, force detection is possible on any position that does not have associated photometric data. The logfile for the analysis is presented in real-time, and all relevant parameters are adopted from the image meta-data without user intervention. Sources may be tagged and named, thus being tracked on the user's profile.

6.5 Future features and optimizations

GrondView and its data ingestion framework are operational within the MPE internal network. The project has therefore completed its goal providing a automated interface to high quality reduced GROND data. Nevertheless, there are several areas that are obvious candidates for improvement. The current workflow for the framework

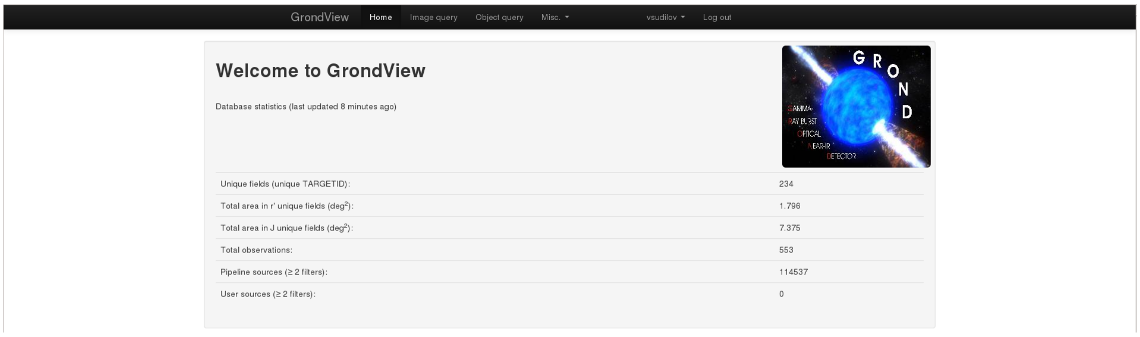

Welcome to GrondView

Database statistics (last updated 8 minutes ago)

Unique fields (unique TARGETID):	234
Total area in r' unique fields (deg^2):	1.796
Total area in J unique fields (deg^2):	7.375
Total observations:	553
Pipeline sources (≥ 2 filters):	114537
User sources (≥ 2 filters):	0

Figure 6.2 The GrondView welcome page, after logging in. The database statistics are refreshed once every 30 minutes.

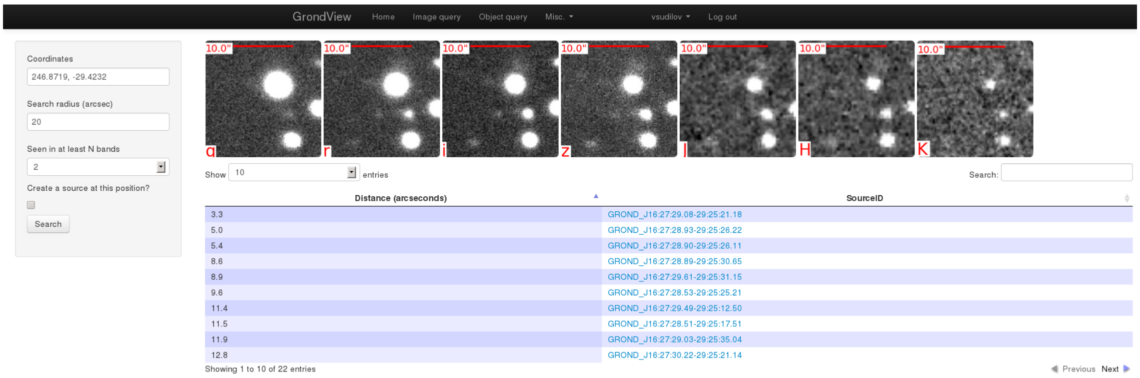

Coordinates: 246.8719, -29.4232

Search radius (arcsec): 20

Seen in at least N bands: 2

Create a source at this position? ☐

Show 10 entries

Search:

Distance (arcseconds)	SourceID
3.3	GROND_J16:27:29.08-29:25:21.18
5.0	GROND_J16:27:28.93-29:25:26.22
5.4	GROND_J16:27:28.90-29:25:26.11
8.6	GROND_J16:27:28.89-29:25:30.65
8.9	GROND_J16:27:29.61-29:25:31.15
9.6	GROND_J16:27:28.53-29:25:25.21
11.4	GROND_J16:27:29.49-29:25:12.50
11.5	GROND_J16:27:28.51-29:25:17.51
11.9	GROND_J16:27:29.03-29:25:35.04
12.8	GROND_J16:27:30.22-29:25:21.14

Showing 1 to 10 of 22 entries

Figure 6.3 Sample output from a positional search of the database.

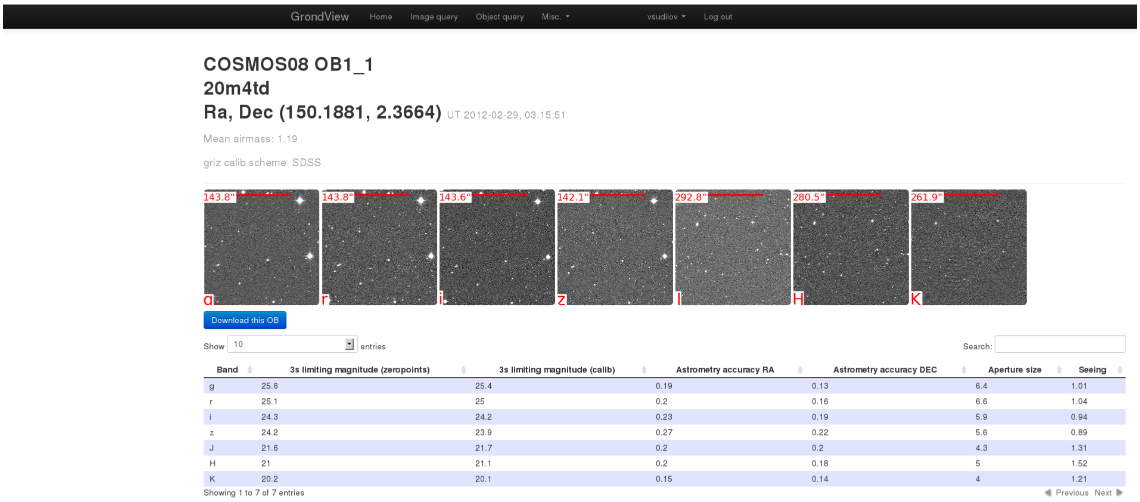

COSMOS08 OB1_1
20m4td
Ra, Dec (150.1881, 2.3664) UT 2012-02-29, 03:15:51

Mean airmass: 1.19

griz calib scheme: SDSS

Band	3s limiting magnitude (zeropoints)	3s limiting magnitude (calib)	Astrometry accuracy RA	Astrometry accuracy DEC	Aperture size	Seeing
g	25.6	25.4	0.19	0.13	6.4	1.01
r	25.1	25	0.2	0.16	6.6	1.04
i	24.3	24.2	0.23	0.19	5.9	0.94
z	24.2	23.9	0.27	0.22	5.6	0.89
J	21.6	21.7	0.2	0.2	4.3	1.31
H	21	21.1	0.2	0.18	5	1.52
K	20.2	20.1	0.15	0.14	4	1.21

Showing 1 to 7 of 7 entries

Figure 6.4 Images and meta-data of the field with targetID COSMOS08 and OB value OB1_1.

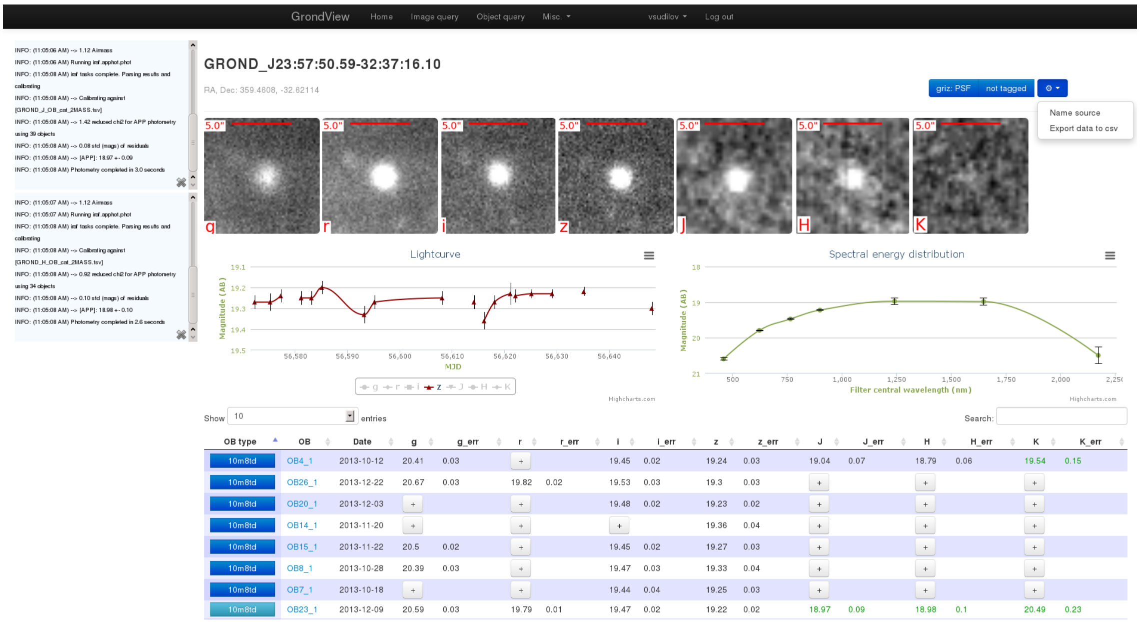

```
INFO: (11:05:06 AM) --> 1.12 Airmass
INFO: (11:05:06 AM) Running iraf.apphot.phot
INFO: (11:05:08 AM) iraf tasks complete. Parsing results and
calibrating
INFO: (11:05:08 AM) --> Calibrating against
[GROND_J_OB_cat_2MASS.tsv]
INFO: (11:05:08 AM) --> 1.42 reduced chi2 for APP photometry
using 39 objects
INFO: (11:05:08 AM) --> 0.08 std (mags) of residuals
INFO: (11:05:08 AM) --> [APP]: 18.97 +- 0.09
INFO: (11:05:08 AM) Photometry completed in 3.0 seconds
```

```
INFO: (11:05:07 AM) --> 1.12 Airmass
INFO: (11:05:07 AM) Running iraf.apphot.phot
INFO: (11:05:08 AM) iraf tasks complete. Parsing results and
calibrating
INFO: (11:05:08 AM) --> Calibrating against
[GROND_H_OB_cat_2MASS.tsv]
INFO: (11:05:08 AM) --> 0.92 reduced chi2 for APP photometry
using 34 objects
INFO: (11:05:08 AM) --> 0.10 std (mags) of residuals
INFO: (11:05:08 AM) --> [APP]: 18.98 +- 0.10
INFO: (11:05:08 AM) Photometry completed in 2.6 seconds
```

GROND_J23:57:50.59-32:37:16.10

RA, Dec: 359.4608, -32.62114

OB type	OB	Date	g	g_err	r	r_err	i	i_err	z	z_err	J	J_err	H	H_err	K	K_err
10m8td	OB4_1	2013-10-12	20.41	0.03	+		19.45	0.02	19.24	0.03	19.04	0.07	18.79	0.06	19.54	0.15
10m8td	OB26_1	2013-12-22	20.67	0.03	19.82	0.02	19.53	0.03	19.3	0.03	+		+		+	
10m8td	OB20_1	2013-12-03	+		+		19.48	0.02	19.23	0.02	+		+		+	
10m8td	OB14_1	2013-11-20	+		+		+		19.36	0.04	+		+		+	
10m8td	OB15_1	2013-11-22	20.5	0.02	+		19.45	0.02	19.27	0.03	+		+		+	
10m8td	OB8_1	2013-10-28	20.39	0.03	+		19.47	0.03	19.33	0.04	+		+		+	
10m8td	OB7_1	2013-10-18	+		+		19.44	0.04	19.25	0.03	+		+		+	
10m8td	OB23_1	2013-12-09	20.59	0.03	19.79	0.01	19.47	0.02	19.22	0.02	18.97	0.09	18.98	0.1	20.49	0.23

Figure 6.5 Detail page of a source. Force detection has been run, with the output updated in the table and graphs in real time. The output from the analysis is also updated in real time on the left panel.

is as follows:

1. Obtain data from USB media
2. Start a `bulk_reduce.py` process
3. Manually verify data with `grond_dataQA.py`
4. Upload and ingest the data to GrondView by invoking `pipeline_push.py`
5. Clean the staging directory by invoking `pipeline_clean.py`

Though this process provides a standard framework for data reduction and ingestion, it still requires human intervention to invoke the next step at the appropriate time. One obvious improvement is to make steps 1-2 and 4-5 completely event driven, and notify the user to perform step 3 at the appropriate time.

A large limitation of this framework is also the rate at which data are reduced and analyzed. Performance could be increased dramatically by optimizing our data reduction pipeline, and by performing reductions in parallel via forking processes.

Though the GrondView positional search is valuable, this is only one (albeit one of the most common) way a scientist searches for data products. Search by magnitudes, colors, or names could also be trivially implemented as search strategies. Additionally, constructing a domain-specific language (DSL) that would allow a proxied query to the main database is also possible. The SDSS CasJobs has implemented this via their SQL search tools, granting scientists the power to query the dataset in extremely specific ways. Constructing such a DSL in the Django framework is relatively straightforward with python lex/yacc[2].

---

[2] See i.e. presentation at DjangoCon 2012, “Implementing Domain Specific-Languages in Django Applications”, by Matthieu Amiguet

Chapter 7

Summary and outlook

We have introduced the so-called MgII issue, which is based on observations of intervening MgII absorption line systems in GRB and quasar sight-lines. At the time of this writing, it remains unclear why there are more MgII lines detected in the high resolution GRB afterglow spectra relative to SDSS quasar spectra. We have reviewed several popular theories from the literature that could account for this difference, including

- Gravitational lensing of GRB afterglows by MgII absorbers
- Intrinsic absorbers misidentified as intervening, perhaps ejected as part of the GRB itself
- Dust extinction bias affecting the sample selection of object follow-up, especially if MgII hosts a significant amount of dust, and
- MgII absorbers that partially cover the beam of the background source, potentially lowering W_r measurements.

We have shown that none of these possible explanations can account for such an observational discrepancy individually. However, since each effect is independent, there is nothing preventing a combination of two or more to reduce the significance of the MgII observations.

Instead of testing these hypotheses, we have tested for a signature of the MgII discrepancy in image data. The MgII discrepancy, originally a spectroscopic and thus *radial* result, should also have a signature in image data if MgII absorbers correspond to bright enough galaxies. With this in mind, we probe the *transverse* dimension of this question by calculating the angular two point GRB-galaxy correlation function. We use five years of data obtained with GROND to construct a deep and homogeneous galaxy catalog using χ^2 template fitting of spectral energy distributions. We increase the sample depth by 4 magnitudes by adding Spitzer data with which GROND has coincident coverage. After confirming the validity of our source extraction and classification method with the COSMOS and SDSS catalogs, we do not find any signal of anomalous clustering in either sample from the two point correlation function.

These results show that there is no excess of bright galaxies in close angular separations to GRB afterglow positions. As MgII tends to trace DLAs and thus normal field galaxies, we conclude that these putative galaxies are likely too dim to be sampled in our survey. This result offers tentative support to the conclusions made by Cucchiara et al. (2013) that the MgII problem exists only in the sample of GRB afterglow spectra taken by a high resolution instruments. Generally, high resolution spectroscopy is performed on brighter targets as compared to low resolution spectroscopy. If MgII is more frequently detected in high resolution spectra than in low resolution spectra, then one should expect that the counterparts to the MgII absorbers are also dim. Unfortunately, the statistical non-detection of these counterparts in our analysis prevents us from quantifying this effect any more specific than the limiting magnitudes of the surveys.

The results of the clustering analysis presented in this work imply that the MgII issue exists at the edge or beyond the sensitivity limits of current samples of GRB afterglow imaging. The most positive interpretation of this result is that imaging of GRB fields does not suffer from the same biases as afterglow spectroscopy, and thus represents a more 'trustworthy' dataset. Combining GRB imaging and spectroscopic datasets will likely be extremely valuable with this knowledge, as these results imply that, if applicable, one may likely use the imaging as a standard with which to compare spectroscopy results. On the other hand, if the luminosity distribution of the galaxies that host metal absorption line systems peaks past the sensitivity limit of our survey, then higher sensitivity surveys like the one we have performed must be performed. Although observationally expensive, increasing the sample of absorbers with confirmed counterparts would best address this question.

The first of ESO's "second-generation" instruments at the VLT, XSHOOTER, saw first light in 2009. XSHOOTER is a optical and NIR medium resolution spectrograph (Vernet et al. 2011). Since its first light, a significant amount of observing time has been detected to measuring GRB afterglow spectra. As more of this data become public, it becomes increasingly attractive to construct a sample of metal absorption line systems from the instrument. A rough estimate is that such a sample would increase the number of GRB-MgII absorbers by at least factor of 10. Importantly, these spectra would have uniform selection criteria, distinct from the current sample of GRB afterglow spectra. A careful analysis is likely to yield information relevant to the MgII issue, especially if the MgII issue depends on instrumental capabilities or observational strategy.

Bibliography

Adelman-McCarthy, J. K., Agüeros, M. A., Allam, S. S., et al. 2008, ApJS, 175, 297

Allen, D. A. 1976, MNRAS, 174, 29P

Arnouts, S., Cristiani, S., Moscardini, L., et al. 1999, MNRAS, 310, 540

Atteia, J.-L., Barat, C., Hurley, K., et al. 1987, ApJS, 64, 305

Berger, E. 2007, ApJ, 670, 1254

Berger, E., Penprase, B. E., Cenko, S. B., et al. 2006, ApJ, 642, 979

Berlind, A. A. & Weinberg, D. H. 2002, ApJ, 575, 587

Bertin, E. & Arnouts, S. 1996, A&AS, 117, 393

Bohlin, R. C., Colina, L., & Finley, D. S. 1995, AJ, 110, 1316

Boksenberg, A., Sargent, W. L. W., & Rauch, M. 2003, ArXiv Astrophysics e-prints

Borgeest, U., von Linde, J., & Refsdal, S. 1991, A&A, 251, L35

Bornancini, C. G., Martínez, H. J., Lambas, D. G., et al. 2004, ApJ, 614, 84

Brainerd, J. J., Meegan, C. A., Briggs, M. S., Pendleton, G. N., & Brock, M. N. 1995, ApJL, 441, L39

Briggs, M. S., Paciesas, W. S., Pendleton, G. N., et al. 1996, ApJ, 459, 40

Bromm, V. & Loeb, A. 2002, ApJ, 575, 111

Bromm, V. & Loeb, A. 2003, ApJ, 596, 34

Calzetti, D., Kinney, A. L., & Storchi-Bergmann, T. 1994, ApJ, 429, 582

Cavallo, G. & Rees, M. J. 1978, MNRAS, 183, 359

Chen, H.-W., Perley, D. A., Pollack, L. K., et al. 2009, ApJ, 691, 152

Chen, H.-W., Prochaska, J. X., Bloom, J. S., & Thompson, I. B. 2005, ApJL, 634, L25

Cline, T. L., Desai, U. D., Klebesadel, R. W., & Strong, I. B. 1973, ApJL, 185, L1

Costa, E., Feroci, M., Piro, L., et al. 1997a, IAU Circ., 6649, 1

Costa, E., Frontera, F., Heise, J., et al. 1997b, Nature, 387, 783

Cucchiara, A., Prochaska, J. X., Zhu, G., et al. 2013, ApJ, 773, 82

Dekker, H., D'Odorico, S., Kaufer, A., Delabre, B., & Kotzlowski, H. 2000, in Society of Photo-Optical Instrumentation Engineers (SPIE) Conference Series, Vol. 4008, Optical and IR Telescope Instrumentation and Detectors, ed. M. Iye & A. F. Moorwood, 534–545

D'Elia, V., Fiore, F., Meurs, E. J. A., et al. 2007, A&A, 467, 629

Dickinson, H. & Tamarkin, P. 1965, IEEE, 53, 1921

Dupree, A. K., Falco, E., Prochaska, J. X., Chen, H.-W., & Bloom, J. S. 2006, GRB Coordinates Network, 4969, 1

Ellison, S. L. 2000, PhD thesis, European Southern Observatory, Chile

Ellison, S. L., Churchill, C. W., Rix, S. A., & Pettini, M. 2004, ApJ, 615, 118

Ellison, S. L., Vreeswijk, P., Ledoux, C., et al. 2006, MNRAS, 372, L38

Fan, Z., Cao, X., & Gu, M. 2006, ApJ, 646, 8

Fazio, G. G., Hora, J. L., Allen, L. E., et al. 2004, ApJS, 154, 10

Fishman, G. J., Meegan, C. A., Wilson, R. B., et al. 1994, ApJS, 92, 229

Fitzpatrick, E. L. 1986, AJ, 92, 1068

Fox, D. B., Frail, D. A., Price, P. A., et al. 2005, Nature, 437, 845

Frank, S., Bentz, M. C., Stanek, K. Z., et al. 2007, Ap&SS, 312, 325

Fynbo, J. P. U., Starling, R. L. C., Ledoux, C., et al. 2006, A&A, 451, L47

Gehrels, N., Chincarini, G., Giommi, P., et al. 2004, ApJ, 611, 1005

Greiner, J., Bornemann, W., Clemens, C., et al. 2008, PASP, 120, 405

Greiner, J., Krühler, T., Fynbo, J. P. U., et al. 2009, ApJ, 693, 1610

Greiner, J., Krühler, T., Klose, S., et al. 2011, A&A, 526, A30

Groth, E. J. & Peebles, P. J. E. 1977, ApJ, 217, 385

Hamann, F., Korista, K. T., & Morris, S. L. 1993, ApJ, 415, 541

Hurley, K., Costa, E., Feroci, M., et al. 1997, IAU Circ., 6594, 1

Ilbert, O., Arnouts, S., McCracken, H. J., et al. 2006, A&A, 457, 841

Ilbert, O., Capak, P., Salvato, M., et al. 2009, ApJ, 690, 1236

Jakobsson, P., Fynbo, J. P. U., Paraficz, D., et al. 2005, GRB Coordinates Network, 4017, 1

Jakobsson, P., Hjorth, J., Malesani, D., et al. 2012, ApJ, 752, 62

Junkkarinen, V. T., Cohen, R. D., Beaver, E. A., et al. 2004, ApJ, 614, 658

Kistler, M. D., Yüksel, H., Beacom, J. F., Hopkins, A. M., & Wyithe, J. S. B. 2009, ApJL, 705, L104

Klebesadel, R. W., Strong, I. B., & Olson, R. A. 1973, ApJL, 182, L85

Krühler, T., Greiner, J., Schady, P., et al. 2011, A&A, 534, A108

Landy, S. D. & Szalay, A. S. 1993, ApJ, 412, 64

Ledoux, C., Vreeswijk, P., Ellison, S., et al. 2005, GRB Coordinates Network, 3860, 1

Ledoux, C., Vreeswijk, P., Smette, A., Jaunsen, A., & Kaufer, A. 2006, GRB Coordinates Network, 5237, 1

Lee, K.-S., Giavalisco, M., Gnedin, O. Y., et al. 2006, ApJ, 642, 63

Lewis, G. F. & Ibata, R. A. 2003, MNRAS, 340, 562

Lithwick, Y. & Sari, R. 2001, ApJ, 555, 540

Lopez, S., Barrientos, L. F., Lira, P., et al. 2008, ApJ, 679, 1144

MacFadyen, A. I. & Woosley, S. E. 1999, ApJ, 524, 262

Matz, S. M., Forrest, D. J., Vestrand, W. T., et al. 1985, ApJL, 288, L37

Mazets, E. P., Golenetskii, S. V., Ilinskii, V. N., et al. 1981, Ap&SS, 80, 3

Ménard, B., Nestor, D., Turnshek, D., et al. 2008, MNRAS, 385, 1053

Mészáros, P. 2002, ARA&A, 40, 137

Mészáros, P. 2006, Reports on Progress in Physics, 69, 2259

Metzger, M. R., Djorgovski, S. G., Kulkarni, S. R., et al. 1997, Nature, 387, 878

Monet, D. G., Levine, S. E., Canzian, B., et al. 2003, AJ, 125, 984

Nardini, M., Ghisellini, G., Ghirlanda, G., et al. 2006, A&A, 451, 821

Paczynski, B. & Proszynski, M. 1986, ApJ, 302, 519

Panaitescu, A. & Kumar, P. 2000, ApJ, 543, 66

Peebles, P. J. E. 1980, The large-scale structure of the universe

Pickles, A. J. 1998, PASP, 110, 863

Piran, T. 1999, Physics Reports, 314, 575

Piranomonte, S., D'Elia, V., Ward, P., Fiore, F., & Meurs, E. J. A. 2006, Nuovo Cimento B Serie, 121, 1561

Porciani, C., Viel, M., & Lilly, S. J. 2007, ApJ, 659, 218

Prevot, M. L., Lequeux, J., Prevot, L., Maurice, E., & Rocca-Volmerange, B. 1984, A&A, 132, 389

Prochaska, J. X., Chen, H.-W., Bloom, J. S., et al. 2005, GRB Coordinates Network, 3732, 1

Prochter, G. E., Prochaska, J. X., & Burles, S. M. 2006a, ApJ, 639, 766

Prochter, G. E., Prochaska, J. X., Chen, H.-W., et al. 2006b, ApJL, 648, L93

Rapoport, S., Onken, C. A., Schmidt, B. P., et al. 2012, ApJ, 754, 139

Rapoport, S., Onken, C. A., Wyithe, J. S. B., Schmidt, B. P., & Thygesen, A. O. 2013, ApJ, 766, 23

Rees, M. J. & Meszaros, P. 1992, MNRAS, 258, 41P

Rees, M. J. & Meszaros, P. 1994, ApJL, 430, L93

Ricker, G. R., Atteia, J.-L., Crew, G. B., et al. 2003, in American Institute of Physics Conference Series, Vol. 662, Gamma-Ray Burst and Afterglow Astronomy 2001: A Workshop Celebrating the First Year of the HETE Mission, ed. G. R. Ricker & R. K. Vanderspek, 3–16

Ross, N. P., Shen, Y., Strauss, M. A., et al. 2009, ApJ, 697, 1634

Salpeter, E. E. 1964, ApJ, 140, 796

Salvato, M., Hasinger, G., Ilbert, O., et al. 2009, ApJ, 690, 1250

Salvato, M., Ilbert, O., Hasinger, G., et al. 2011, ApJ, 742, 61

Savaglio, S., Fall, S. M., & Fiore, F. 2003, ApJ, 585, 638

Schlafly, E. F. & Finkbeiner, D. P. 2011, ApJ, 737, 103

Schlegel, D. J., Finkbeiner, D. P., & Davis, M. 1998, ApJ, 500, 525

Schulze, S., Fynbo, J. P. U., Milvang-Jensen, B., et al. 2012, A&A, 546, A20

Singer, S. 1965, IEEE, 53, 1935

Skrutskie, M. F., Cutri, R. M., Stiening, R., et al. 2006, AJ, 131, 1163

Songaila, A. 2005, AJ, 130, 1996

Songaila, A. 2006, AJ, 131, 24

Steidel, C. C., Giavalisco, M., Pettini, M., Dickinson, M., & Adelberger, K. L. 1996, ApJL, 462, L17

Strong, I. B. & Klebesadel, R. W. 1974, Nature, 251, 396

Sudilovsky, V., Greiner, J., Rau, A., et al. 2013, A&A, 552, A143

Sudilovsky, V., Savaglio, S., Vreeswijk, P., et al. 2007, ApJ, 669, 741

Sudilovsky, V., Smith, D., & Savaglio, S. 2009, ApJ, 699, 56

van Paradijs, J., Groot, P. J., Galama, T., et al. 1997, Nature, 386, 686

Vedrenne, G. 1991, Annals of the New York Academy of Sciences, 647, 556

Vergani, S. D., Petitjean, P., Ledoux, C., et al. 2009, A&A, 503, 771

Vernet, J., Dekker, H., D'Odorico, S., et al. 2011, A&A, 536, A105

Vladilo, G. & Péroux, C. 2005, A&A, 444, 461

Vreeswijk, P. M., Ledoux, C., Smette, A., et al. 2007, A&A, 468, 83

Wang, J. & Wei, J.-Y. 2010, Research in Astronomy and Astrophysics, 10, 533

Wild, V., Hewett, P. C., & Pettini, M. 2006, MNRAS, 367, 211

Willott, C. J., Simpson, C., Almaini, O., et al. 2004, ApJ, 610, 140

Woosley, S. E. 1993, ApJ, 405, 273

Wright, E. L. 2006, PASP, 118, 1711

Wyithe, J. S. B., Winn, J. N., & Rusin, D. 2003, ApJ, 583, 58

York, D. G., Khare, P., Vanden Berk, D., et al. 2006, MNRAS, 367, 945

Zel'dovich, Y. B. & Novikov, I. D. 1964, Soviet Physics Doklady, 9, 246

Acknowledgments

I would like to thank:

The staff at the MPE and La Silla Observatory, and the GROND team for outstanding support.

Donald Smith and Rex Adelberger, whose enthusiasm and intelligence inspired me to pursue physics.

Sandra Savaglio, for being an extremely generous and caring mentor in research.

Jochen Greiner, who gave me the opportunity to do science first hand at a world leading research institute and observatory, and for encouraging me to pursue my interests.

Jonny Elliott, who has been an understanding peer and compassionate friend during my time at the MPE.

My parents, John and Luba, who have never failed in supporting me during easy or difficult times.

I would like to thank my wife, Genevieve, whose company is always the best part of the day.

Without all of you, this work would not have been possible. I am grateful for the positive impact you all have made on me.